

# NONLINEAR EVOLUTION OF GLOBAL HYDRODYNAMIC SHALLOW-WATER INSTABILITY IN SOLAR TACHOCLINE

MAUSUMI DIKPATI

*High Altitude Observatory, National Center for Atmospheric Research<sup>1</sup>, 3080 Center Green, Boulder, Colorado 80301; dikpati@ucar.edu*

## ABSTRACT

We present a fully nonlinear hydrodynamic 'shallow water' model of the solar tachocline. The model consists of a global spherical shell of differentially rotating fluid, which has a deformable top, thus allowing motions in radial directions along with latitude and longitude directions. When the system is perturbed, in the course of its nonlinear evolution it can generate unstable low-frequency shallow-water shear modes from the differential rotation, high-frequency gravity waves, and their interactions. Radiative and overshoot tachoclines are characterized in this model by high and low effective gravity values respectively. Building a semi-implicit spectral scheme containing very low numerical diffusion, we perform nonlinear evolution of shallow-water modes. Our first results show that, (i) high latitude jets or polar spin-up occurs due to nonlinear evolution of unstable hydrodynamic shallow-water disturbances and differential rotation, (ii) Reynolds stresses in the disturbances together with changing shell-thickness and meridional flow are responsible for the evolution of differential rotation, (iii) disturbance energy primarily remains concentrated in the lowest longitudinal wavenumbers, (iv) an oscillation in energy between perturbed and unperturbed states occurs due to evolution of these modes in a nearly dissipation-free system, and (v) disturbances are geostrophic, but occasional nonadjustment in geostrophic balance can occur, particularly in the case of high effective gravity, leading to generation of gravity waves. We also find that a linearly stable differential rotation profile remains nonlinearly stable.

## 1. Introduction

The solar tachocline plays a fundamental role in governing the dynamics and evolution of the Sun's interior magnetic fields, manifestations of which are observed at the solar surface.

---

<sup>1</sup>The National Center for Atmospheric Research is sponsored by the National Science Foundation.

The tachocline is a very thin ( $\sim 0.03R$ ) transition layer at the base of the convection zone through which the solar differential rotation changes from latitudinal in the convection zone to a uniform core rotation. This layer contains strong radial and weak latitudinal differential rotation.

Due to existence of both radial and latitudinal shear in the tachocline, the study of its dynamics and physics is complex. Analysis of tachocline hydro- and magnetohydrodynamics have proceeded in two different ways: the first way treats the thin tachocline explicitly as a full three dimensional multilayered spherical system (see, for example, Chan, Liao & Zhang (2008)). The other way is to treat the tachocline as a one-layer system. The multilayer system has been used to study the dynamics of both shears, radial and latitudinal, while the one-layer system has been applied to examine the dynamics and stability of only the latitudinal shear. Over the past decade, various models have been built for global HD/MHD of the tachocline latitudinal shear – 2D, quasi-3D shallow-water systems and 3D thin-shell primitive equation systems, under both the Boussinesq and hydrostatic approximations.

The linear and nonlinear calculations of HD/MHD instability of tachocline latitudinal shear have been performed in great detail for a 2D (latitude-longitude) system. These studies led to the following major outcomes: (i) solar tachocline latitudinal shear is hydrodynamically stable in pure 2D systems (Watson 1981; Dziembowski & Kosovichev 1987; Charbonneau, Dikpati & Gilman 1999; Garaud 2001); (ii) MHD shear instability with longitudinal wavenumber  $m = 1$  to 7 sets in and persists in the solar tachocline in the presence of a wide range of toroidal field profiles (from broad to narrow bands), amplitudes and latitude-locations (Gilman & Fox 1997; Dikpati & Gilman 1999; Gilman & Dikpati 2002); (iii) axisymmetric HD/MHD instability does not, or more precisely, cannot exist in 2D; (iv) as consequences of the nonlinear evolution of this instability, broad toroidal fields open up into "clam-shell" patterns (Cally 2001), whereas narrow bands tip (Cally, Dikpati & Gilman 2003).

We now know that the 2D results are robust. All of them obtained from linear analysis have been found to appear in more complex quasi-3D 'shallow-water' systems (Dikpati & Gilman 2001; Gilman & Dikpati 2002; Dikpati, Gilman & Rempel 2003), in which the third dimension is generally included in a restricted way, namely the upper boundary of the shallow fluid-shell is allowed to vary with latitude, longitude and time so that the radial motions can occur. Intuitively it is expected that the inclusion of the third dimension would produce some other unstable modes that are purely characteristic of 3D because, in addition to the kinetic and magnetic energy reservoirs due to the presence of differential rotation and magnetic field, 3D systems allow energy extraction from the potential energy reservoir, particularly when the effective gravity ( $G$ ) of the system is low.  $G$  is a measure of the subadiabatic

stratification of the fluid layer; low  $G$  can allow more deformation of the fluid-layer’s top surface. In linear studies, it was indeed found that a hydrodynamically stable 2D tachocline can be unstable to quasi-3D perturbations, due to the presence of this additional energy source in a shallow-water model (Dikpati & Gilman 2001).

Many idealized shallow-water models have been built over the past century, since the first, single-layer model by Hough (1898). For studying the mid-latitude oceanic tides and atmospheric zonal flows and meridional circulation, multi-layer shallow-water models are used (Huang & Pedlosky 1998; Hurlburt & Hogan 2008). Shallow water models are also being used for operational forecasts of El Nino and La Nina (Philander & Fedorov 2003).

Shallow water theory was applied to the global solar tachocline by Gilman (2000), who first formulated an MHD analog of a shallow-water system. Since then, all global studies of HD/MHD shallow-water instabilities in the solar tachocline have been performed in the linear regime. Nonetheless, even within the scope of a linear model, the upward bulging of a magnetized shallow fluid layer created at certain longitudes, by growing modes with low-longitudinal wavenumbers, can provide a plausible explanation of the Sun’s “active longitudes” (see Dikpati & Gilman (2005) for details). This linear model was able to simulate active longitudes up to 15 Carrington Rotations, after which nonlinear interactions among the unstable modes start playing important roles. In order to be able to simulate active longitudes for one full solar cycle and several solar cycles, it is necessary to study the nonlinear evolution of the aforementioned instability in the tachocline fluid layer.

Over the past decade, several 3D thin-shell and full 3D HD and MHD models for linear analysis of tachocline shear instabilities have been built (Cally 2001; Zhang, Liao & Schubert 2003; Arlt, Sule & Rüdiger 2005; Gilman, Dikpati & Miesch 2007). However, unlike many studies of nonlinear evolution of shallow-water instabilities in the oceanic and atmospheric context (see, e.g. Poulin & Flierl (2003)), there exist only a few studies of the nonlinear evolution of 3D MHD instabilities in the solar context, using 3D thin-shell models (Miesch, Gilman & Dikpati 2007; Hollerbach & Cally 2009). Although in a shallow-water model the radial dimension of the fluid layer is included in a simplified way by allowing the layer’s thickness to vary with latitude, longitude and time, it is not as restricted compared to a full 3D MHD system as it might appear. Rempel & Dikpati (2003) have shown that an MHD shallow-water approach is a first-order approximation of a full MHD equilibrium in which the magnetic curvature stress is balanced by a latitudinal pressure gradient for a strongly subadiabatic stratification and by modification in the shear flow for a weakly subadiabatic stratification. The height deformation of the top surface layer in the shallow-water approach corresponds to the deformation of the surfaces of constant entropy required for latitudinal force balance in the full MHD approach. Thus using a shallow water system for

the Sun, specifically for the solar tachocline, can help reduce the complexity of a full 3D MHD system without much affecting the basic physics behind the global dynamics of the fluid layer.

Putting aside the added complexity due to the presence of magnetic fields, we first focus on the nonlinear evolution of shear instability in an unmagnetized solar tachocline and find out how the tachocline latitudinal differential rotation profile can evolve with time and get modified due to the influence of this instability. In pure 2D calculations, the jets were seen to form around the locations of the singular points arising from the coincidence between the Doppler-shifted phase-speed of the unstable modes and the shear-speed of the system, or the Alfvénic singular points in the case of magnetized tachocline (Cally, Dikpati & Gilman 2004). Along with the exploration of jet-formation on unperturbed differential rotation profiles due to the nonlinear evolution of hydrodynamic shear instability, another major aim of this paper is to study the nonlinear evolution of the bulging and depression of the fluid layer in conjunction with the shear flow pattern, or in other words, the exchanges between the kinetic and potential energies of the system.

We will present the mathematical formulation including equations and solution techniques in §2 and in the Appendix, and the implementation of spectral viscosity in §3. In the description of results in §4 we will present in the first subsection how the energy spectrum develops, i.e. how the total energy gets distributed in different longitudinal wavenumbers and how they evolve with time. The subsequent subsections of §4 will focus on the evolution of the Sun’s longitude-averaged differential rotation and the height profile, the energy exchanges between kinetic and potential energy reservoirs, and the evolution of flow and deformation of the fluid layer on the latitude-longitude surface. We will summarize our findings in §5.

## 2. Mathematical Formulation

### 2.1. Governing equations

Hydrodynamic shallow-water equations were built for studying global atmospheric and oceanic dynamics; they exist in the literature in various forms, for example see Pedlosky (1987). Following that, Dikpati & Gilman (2001) described the hydrodynamic shallow-water equations, along with the usual assumptions and approximations in their §2.1 and §2.2 and solved them in the linear regime. Briefly, in a shallow water model the velocity ( $\mathbf{V}$ ) of the fluid can be defined as  $\mathbf{V} = u\hat{\boldsymbol{\lambda}} + v\hat{\boldsymbol{\phi}} + w\hat{\mathbf{r}}$ , where  $u$  and  $v$  are the horizontal velocity components in longitude ( $\lambda$ ) and latitude ( $\phi$ ) respectively, and  $w$  is the radial velocity. In the

shallow water approximation,  $u$  and  $v$  are independent of depth, and  $w$  is a linear function of depth. For a shallow fluid layer with a rigid bottom and a deformable top, the maximum vertical velocity will be at the top.

Due to the thinness of the tachocline compared to the solar radius, the divergence of radius and the density variation within the shallow fluid layer are ignored in the momentum and mass-continuity equations. All time scales of the system are considered much longer than the acoustic time scale. With these assumptions, the hydrodynamic shallow water equations for a single-layer tachocline can be derived from the mass continuity and momentum equations (see Dikpati & Gilman (2001) for detailed derivation). In order to study the nonlinear evolution of the hydrodynamic shallow-water instability in the solar tachocline, we start from the equations (4), (5) and (8) of Dikpati & Gilman (2001) and rewrite the nonlinear dimensional hydrodynamic shallow-water equations in the rotating frame as,

$$\frac{\partial u}{\partial t} = \frac{v}{r_0 \cos \phi} \left[ \frac{\partial v}{\partial \lambda} - \frac{\partial}{\partial \phi}(u \cos \phi) \right] - \frac{1}{r_0 \cos \phi} \frac{\partial}{\partial \lambda} \left( \frac{u^2 + v^2}{2} \right) - \frac{gH}{r_0 \cos \phi} \frac{\partial h}{\partial \lambda} + 2\omega_c v \sin \phi, \quad (1)$$

$$\frac{\partial v}{\partial t} = -\frac{u}{r_0 \cos \phi} \left[ \frac{\partial u}{\partial \lambda} - \frac{\partial}{\partial \phi}(u \cos \phi) \right] - \frac{1}{r_0} \frac{\partial}{\partial \phi} \left( \frac{u^2 + v^2}{2} \right) - \frac{gH}{r_0} \frac{\partial h}{\partial \phi} - 2\omega_c u \sin \phi, \quad (2)$$

$$\frac{\partial}{\partial t}(1 + h) = -\frac{1}{r_0 \cos \phi} \frac{\partial}{\partial \lambda} ((1 + h)u) - \frac{1}{r_0 \cos \phi} \frac{\partial}{\partial \phi} ((1 + h)v \cos \phi), \quad (3)$$

in which  $u$  and  $v$  are the horizontal velocity components in longitude ( $\lambda$ ) and latitude ( $\phi$ ), and  $h$  is the deformable top surface.

We make equations (1-3) dimensionless by choosing the radius of the shell ( $r_0$ ) as the length-scale and the inverse of the core rotation rate ( $\omega_c^{-1}$ ) as the time-scale of the system; thus the thickness of the fluid layer representing either the radiative or the overshoot part of the solar tachocline should be between 0.01 and 0.05 dimensionless units, and one year time will correspond to about 100 dimensionless units. The nondimensional equations are

$$\frac{\partial u}{\partial t} = \frac{v}{\cos \phi} \left[ \frac{\partial v}{\partial \lambda} - \frac{\partial}{\partial \phi}(u \cos \phi) \right] - \frac{1}{\cos \phi} \frac{\partial}{\partial \lambda} \left( \frac{u^2 + v^2}{2} \right) - G \frac{1}{\cos \phi} \frac{\partial h}{\partial \lambda} + 2\omega_c v \sin \phi, \quad (4)$$

$$\frac{\partial v}{\partial t} = -\frac{u}{\cos \phi} \left[ \frac{\partial u}{\partial \lambda} - \frac{\partial}{\partial \phi}(u \cos \phi) \right] - \frac{\partial}{\partial \phi} \left( \frac{u^2 + v^2}{2} \right) - G \frac{\partial h}{\partial \phi} - 2\omega_c u \sin \phi, \quad (5)$$

$$\frac{\partial}{\partial t}(1+h) = -\frac{1}{\cos\phi}\frac{\partial}{\partial\lambda}((1+h)u) - \frac{1}{\cos\phi}\frac{\partial}{\partial\phi}((1+h)v\cos\phi), \quad (6)$$

in which  $G = gH/r_0^2\omega_c^2$  is the effective gravity. With typical values  $H$ , the pressure scale height, the value of  $G$  is high ( $\geq 10$ ) in the radiative tachocline and low ( $< 1$ ) in the overshoot part of the tachocline.

Due to the pole problem, it is difficult to solve the advective form of shallow-water equations in spherical polar coordinates. It is a fundamental problem for solving numerically the partial differential equations on the sphere, particularly using finite difference methods – certain terms are likely to be unbounded in the neighborhood of the poles. Spectral methods are popular for their high accuracy and their ability to avoid the pole problem. There exists a vast literature on how to avoid the pole problem. We follow here a technique proposed by Swarztrauber (1996) and so we define the vorticity ( $\zeta$ ) and divergence ( $\delta$ ) as

$$\zeta = \frac{1}{\cos\phi} \left[ \frac{\partial v}{\partial\lambda} - \frac{\partial}{\partial\phi}(u\cos\phi) \right], \quad (7a)$$

$$\delta = \frac{1}{\cos\phi} \left[ \frac{\partial u}{\partial\lambda} + \frac{\partial}{\partial\phi}(v\cos\phi) \right], \quad (7b)$$

and rewrite the equations (4-6) as follows:

$$\frac{\partial u}{\partial t} = (\zeta + f)v - \frac{1}{\cos\phi}\frac{\partial}{\partial\lambda} \left[ gh + \frac{1}{2}(u^2 + v^2) \right], \quad (8)$$

$$\frac{\partial v}{\partial t} = -(\zeta + f)u - \frac{\partial}{\partial\phi} \left[ gh + \frac{1}{2}(u^2 + v^2) \right], \quad (9)$$

$$\frac{\partial h}{\partial t} = -(1+h)\delta - \frac{u}{\cos\phi}\frac{\partial h}{\partial\lambda} - v\frac{\partial h}{\partial\phi}, \quad (10)$$

where,  $f = 2\omega_c \sin\phi$  is the Coriolis parameter.

We apply the spectral transform method (Swarztrauber 1996) to solve the Equations (8-10), by expanding the vector field (i.e. the flow) and the scalar field (height) respectively in terms of vector and scalar harmonics. Thus the pole problem can be handled efficiently without raising the order of the equations. The appendix describes in detail the technique used to solve the Equations (8-10).

## 2.2. Description of Initial State, Numerical Algorithm and Spectral Viscosity

We express the solar tachocline latitudinal differential rotation in angular measure,  $\omega$ , so that  $u = \omega \cos\phi$ . From the knowledge of helioseismic observations the mathematical form

of  $\omega$  has been adopted as

$$\omega = s_0 - s_2\mu^2 - s_4\mu^4 - \omega_c, \quad (11)$$

in which  $\omega_c$  represents the solid rotation of the core, and  $s_0$ ,  $s_2$  and  $s_4$  are numerical coefficients.  $(s_2 + s_4)/s_0 \sim 0.3$  represents solar latitudinal differential rotation near the surface, whereas in the radiative part of the tachocline,  $(s_2 + s_4)/s_0 \leq 0.17$  (Charbonneau, Dikpati & Gilman 1999). Detailed parameter surveys in the linear regime (Dikpati & Gilman 2001) have revealed that  $\omega$  becomes unstable to perturbations with longitudinal wavenumbers  $m = 1$  and  $m = 2$  for a wide range of  $s_2$  and  $s_4$  values. In order to focus our study on how this instability evolves in the cases of high and low effective gravity ( $G$ ), we pick an  $\omega$  with  $s_2 = 0.15$ ,  $s_4 = 0.09$  and  $s_0 = 1.051$  so that the pole-to-equator differential rotation is 24%. Linear studies indicate that this differential rotation is hydrodynamically unstable for a wide range of  $G$ . Therefore we can demonstrate the features of the time-evolution of this differential rotation for both high  $G$  and low  $G$  cases, in particular  $G = 10$  and  $0.5$  (Rempel & Dikpati 2003; Dikpati, Gilman & Rempel 2003) which are, respectively, characteristic of radiative and overshoot tachoclines.

We also study a few other cases with 30% and 15% pole-to-equator differential rotation. In all cases we start with an initial reference state profile that is a combination of unperturbed profile and a perturbation with low longitudinal wavenumbers (mostly  $m = 1$  mode), with a specified amplitude with respect to the unperturbed differential rotation.

In all simulations we start from known solutions to the linearized instability equations, rather than from perturbations of arbitrary form, which has the effect of initially filtering gravity waves out of the calculations. But once nonlinearities become important, gravity wave modes can and frequently are excited and subsequently participate in the overall dynamics.

### 2.3. Spectral Viscosity

Spectral methods, despite their accuracy and absence of pole problems, are prone to generating spurious oscillations in physical space and hence a reduction in global accuracy. In the case of nonlinear evolution equations in an idealized, inviscid model like the one we are presently dealing with, spectral methods generate energy cascade from lower to higher wave number modes, which often creates a spectrum with an erroneously high amplitude tail at high longitudinal wavenumbers – the so-called spectral blocking problem, which could eventually lead to a poor energy-conservation during the nonlinear evolution of the system. The traditional approach is to use an artificial horizontal diffusion to deal with these difficulties of spectral methods.

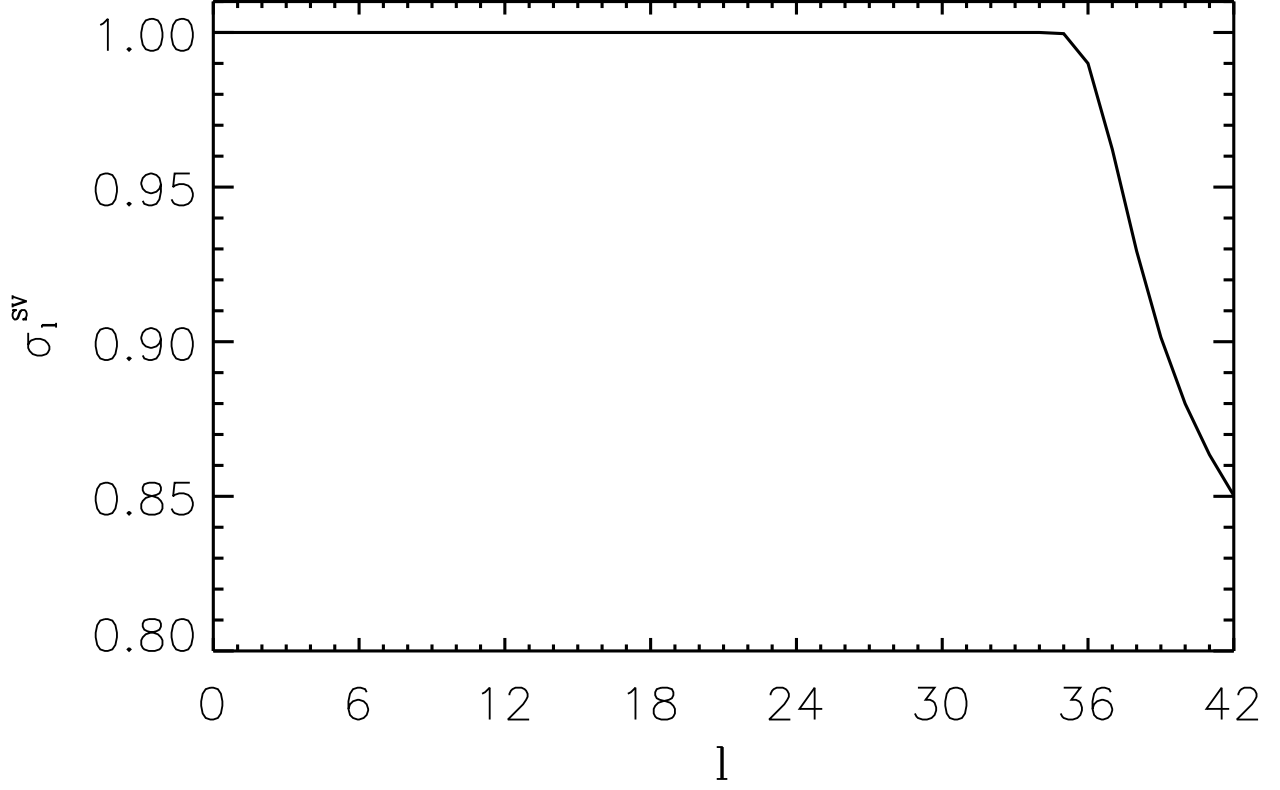


Fig. 1.— Spherical spectral viscosity operator as function of wavenumber  $l$  in Legendre polynomial  $P_l^m$ .

We apply the Spectral Viscosity (SV), as prescribed by Gelb & Gleeson (2001), which is a spherical spectral viscosity operator, able to conserve invariants of the system at no additional computing cost and to retain the high wave number information in the system. The dynamical variables  $a_r^{lm}$ ,  $a_i^{lm}$ ,  $b_r^{lm}$ ,  $b_i^{lm}$ ,  $c_r^{lm}$  and  $c_i^{lm}$  are filtered at each time step using the formula

$$a_r^{lm} = \sigma_l^{SV} a_r^{lm}, \quad (11a)$$

in which

$$\sigma_l^{SV} = \frac{1}{1 + 2\Delta_t \epsilon \hat{q}_l^2 l^2 (l+1)^2}, \quad (11b)$$

with  $\hat{q}_l$  satisfying the following two conditions:

$$\begin{aligned} \hat{q}_l &= 0, \quad \text{for } l \leq l_c, \\ &= \exp\left[-\frac{(l-M)^2}{2(l-l_c)^2}\right], \quad \text{for } l_c < l \leq M, \end{aligned}$$

in which  $M$  is the truncation limit of  $n$ . The  $\epsilon$  and  $l_c$  have been taken to be  $\epsilon = \frac{2}{M^3}$  and  $l_c = 2M^{3/4}$ . The pattern of  $\sigma_l^{SV}$  as function of  $l$  is shown in Figure 1.



In a viscous model for the astrophysical fluid simulations, the use of artificial horizontal diffusion will not be needed, as it would always include the physical diffusion (for example, see Fan et al. (1999)). The comparison between an inviscid model with artificial diffusion and a viscous model without artificial diffusion can be done by using the similar amount of artificial and physical diffusion in respective models. In order to derive an equivalent physical diffusion from the artificial diffusion used in an inviscid model, a plausible experiment can be set up as follows. By switching off all energy sources, such as kinetic energy from shear flow and the potential energy from effective gravity, just the time-rate of the spread of a 2D Gaussian function in latitude-longitude direction can be studied in the presence of an artificial diffusion. The horizontal diffusion, estimated from the rate of spread of 2D Gaussian function, can be used as the amount of physical diffusion in a viscous model without any artificial diffusion. The nonlinear evolution of a shallow-water instability, specifically the spectral blocking issue and the quality of energy conservation from such a viscous model can be compared with that from an inviscid model with artificial diffusion. A forthcoming paper will address this comparison quantitatively.

However, one of the limitations of a single-layer shallow-water model, in both viscous and inviscid cases, is that the horizontal velocities are independent of depth – only the vertical velocity varies with depth. Thus there are no viscous terms that involve radial second derivatives of horizontal velocities in the horizontal components of the momentum equations. In reality, a full 3D tachocline model will be a viscous model. So a multilayer shallow-water model will be needed to connect the layers through some diffusion in the radial direction, as has been done in the case of a full 3D, multilayer tachocline model by Chan, Liao & Zhang (2008). Alternatively, the effect of radial diffusion can be explored by using a Newton’s cooling type formalism in which the radial diffusion terms can be converted into drag terms (for example, see Dikpati, Cally & Gilman (2004)). In future, development of such a model will also help investigate the effect of forcing the differential rotation at the top of the layer.

## 2.4. Adjusting the time step

In order to increase the efficiency of the numerical code, we use an adjustable time step which can be changed (up or down) during the the simulation. If the time step,  $\Delta t$ , is taken large, it may result in poor energy conservation, whereas if it is taken small, it will lead to longer runs that will take many steps and more time to compute. In the course of a computation, if the system is going through an interval near the peak of its potential or kinetic energy, then a somewhat lower time step will ensure better accuracy. At other times

of the evolution, a larger time step can be taken, because that will speed up the computation. Therefore we have implemented a variable time step that is adjustable at each iteration. The scheme for adjusting time step is described below.

We define  $\epsilon$  as the fractional update of a variable— the ratio of the magnitude of the update of that variable and the magnitude of the variable at that time step. When evaluating  $\epsilon$  we exclude those variables whose absolute magnitude is less than  $10^{-4}$ , because the effect of those variables on the physical dynamics at that point in time is very small compared to the normalized variables. Then we evaluate the maximum value of  $\epsilon$  over all the updates at that time step. If the maximum in  $\epsilon$  turns out to be less than 0.005 then we scale up the next time step by a factor of 1.02 of current time step. On the other hand, if the maximum in  $\epsilon$  is greater than 0.005 then we scale down the time step by 0.8 and reevaluate the evolution of the variables at that time step. In this way we limit the amount of maximum update of a variable, and hence the drastic change in the system at a given time step, to achieve good energy conservation over long periods of time.

Values of scale-down and scale-up in the time-step are chosen to be 20% and 2% respectively. These are somewhat arbitrary, but we have found for our present calculations the amount of scale-down in the time-step needs to be larger than that of scale-up. This is because accuracy in the conservation of the energy deteriorates when the system is evolving rapidly.

### 3. Results

In order to present results and physical interpretations in a well-organized fashion, we divide this section into four subsections, which will successively present the convergence test related to the selection of longitudinal wavenumbers, a test for total energy conservation and exchanges among different energy reservoirs, nonlinear evolution of longitude-averaged flow and height profiles, and nonlinear evolution of flow accompanied by deformations of the fluid shell in latitude and longitude.

#### 3.1. Convergence test for truncation in $m$

For the technique described in detail in the appendix, the computation speed largely depends on the number of  $l$ 's and  $m$ 's we select in the basis functions. The total energy is

defined in this system as

$$T_{en} = \int \int d\phi d\theta \cdot \left[ (1 + h) \left( \frac{u^2 + v^2}{2} \right) + \frac{G \cdot h (h + 2)}{2} \right], \quad (12)$$

in which  $u$ ,  $v$  and  $h$  represent longitudinal velocity, latitudinal velocity and height deformation. Since the modes with longitudinal wavenumbers  $m = 1$  and  $2$  are the only modes that are linearly unstable in the solar tachocline, we construct our initial configuration of the flow and height-deformation by using the modes with  $m$  equal to  $2$  at the most.

We calculate the energy distribution at each longitudinal wavenumber  $m$ , using the expression (12), for two  $G$  values, namely  $G = 10$  and  $G = 0.5$ , and plot them in Figures 2(a) and (b) as functions of  $m$ . In both cases we have taken a pole-to-equator differential rotation amplitude of 24% with  $s_2 = 0.15$ ,  $s_4 = 0.09$  in the expression (13). The total energy of the system for different wavenumbers  $m = 1$  through  $10$ , plotted at the time  $t = 0$ ,  $t = 50$  and  $t = 90$  (respectively by black, red and blue diamonds) show that the energy contribution falls off rapidly with  $m$ . At  $t = 0$  the total energy of the system is contained in  $m = 0$  and  $m = 1$ , because that is how we constructed the reference state. which suggests that  $m$  may be truncated at  $6$  or  $7$  with very little loss of accuracy; this speeds up our computation enormously.

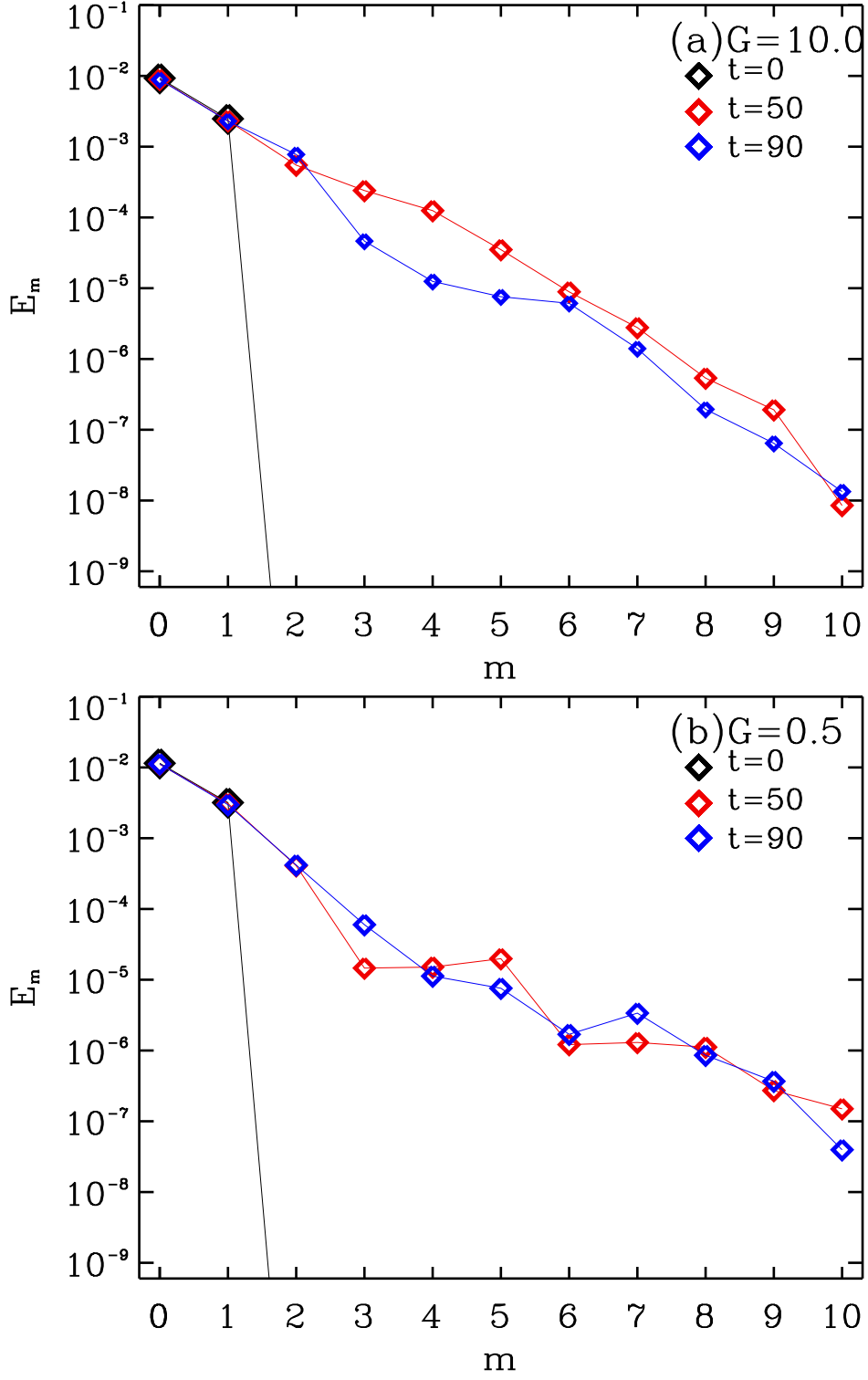


Fig. 2.— Spectrum of total energy as function of longitudinal wavenumber  $m$  at  $t = 0$  (black diamonds), 50 (red diamonds) and 90 (blue diamonds), for (a)  $G = 10$  and (b)  $G = 0.5$ . Note that dimensional time for  $t = 40$  and 90 are respectively 4.8 and 10.8 months.

### 3.2. Evolution of energetics

Because the fluid-shell system with latitudinal differential rotation has its own inherent instability for low-order longitudinal wavenumber modes, in the course of the nonlinear evolution of such a system its unstable modes grow by taking energy from the unperturbed system and thus modifying the system. At a certain point the reference-state system gets modified to the extent that it takes back energy from the perturbations. The cascading of energy to higher longitudinal modes is not significant in this system for  $m$  below 6 or 7; instead a stable oscillation of energy between the reference-state and perturbations develops. Figures 3(a) shows such an oscillation between the reference-state ( $m = 0$ ) kinetic energy ( $\bar{K}$ ) and the perturbation ( $m > 0$ ) kinetic energy ( $K'$ ), for a perturbation of about 40% in the differential rotation (angular measure, i.e.  $u = \omega \cos \theta$ ), for the case of  $G = 0.5$ . Similar oscillations occur in  $G = 10$  case.

The same period and phase of oscillation occurs between the reference state ( $\bar{P}$ ) and perturbation ( $P'$ ) potential energies in the system, but with substantially smaller amplitude than for the kinetic energy. We see that during this oscillation the total energy of the system remains virtually constant, which shows that the numerical viscosity in the system is extremely small. In fact, the total kinetic and total potential energies are separately constant, so that the energy exchanges are strictly between reference state and perturbation energies of the same type.

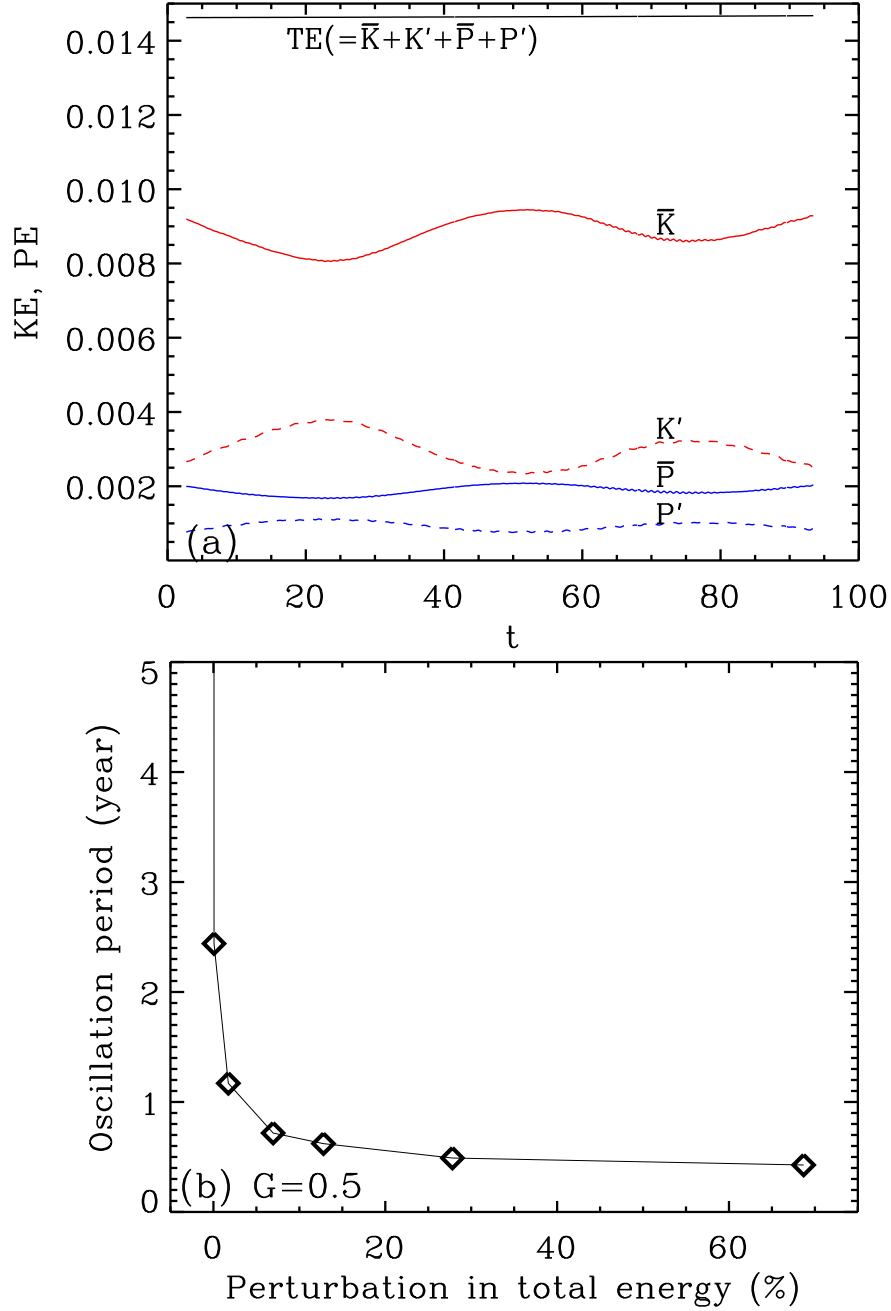


Fig. 3.— Frame (a) shows the evolution of reference state kinetic energy,  $\bar{K}$  (i.e.,  $KE_{m=0}$ , plotted in red solid curve), potential energy,  $\bar{P}$  (i.e.,  $PE_{m=0}$ , blue solid curve), perturbation kinetic energy,  $K'$  (i.e.,  $KE_{m>0}$ , red dashed curve), and potential energy,  $P'$  (i.e.,  $PE_{m>0}$ , blue dashed curve). The energy exchanges between  $\bar{K}$  and  $K'$ , and between  $\bar{P}$  and  $P'$  shows an oscillatory pattern, the frequency of which depends on the amplitude of the perturbation, while total energy, plotted in solid black curve, is conserved. Frame (b) shows the oscillation period of energy exchange between the reference state and perturbation as function of perturbation energy measured as a fraction of the reference state energy of the system.

From equation (56) of Dikpati & Gilman (2001) we can infer that this oscillation is driven by the time dependent Reynolds stress of the perturbations. Initially this stress extracts kinetic energy from the differential rotation, which is modified in such a way as to reduce the energy available for continued growth in the disturbance. But the system then ‘overshoots’ an equilibrium state, resulting at later phases in the oscillation in the perturbations giving back kinetic energy to the differential rotation. Then the perturbations are able to grow again, and the oscillation repeats. In §3.4 we will show how the disturbance structure changes during the oscillation.

Figure 3(b) shows how the oscillation period depends on the initial perturbation amplitude. The relationship is obviously not linear. The process that causes this behavior is also nonlinear. Physically what is happening is that as the initial perturbation amplitude is increased, energy is extracted from the differential rotation at a faster rate. This modifies the differential rotation profile faster to a form that is less unstable to the perturbation and subsequently to a form that extracts energy from the perturbation. This makes the period shorter. There is probably a limit to how short the period can be, as evidenced by the curve in Figure 3b approaching an asymptote in period that is greater than zero.

Conversely for very low initial amplitude the period gets longer, but probably not to infinity because the initial growth is exponential (and the rate is independent of the small amplitude). It simply takes longer for the growing disturbance to reach a point in time at which the feedback from the modified differential rotation is strong enough to limit further growth.

### 3.3. Nonlinear evolution of differential rotation – formation of high-latitude jets

We have seen above that the kinetic and potential energies of the nonlinear shallow water system go through a well defined oscillation. How is this manifested in the changes in the differential rotation profile? Figures 4a,b show its behavior for the same time period, for both high  $G$  (frame a) and low  $G$  (frame b), for a 40% initial disturbance amplitude. Here is plotted the angular velocity in the shell for five later times, compared with the initial profile (black curve). All angular velocities are taken relative to the core rotation rate.

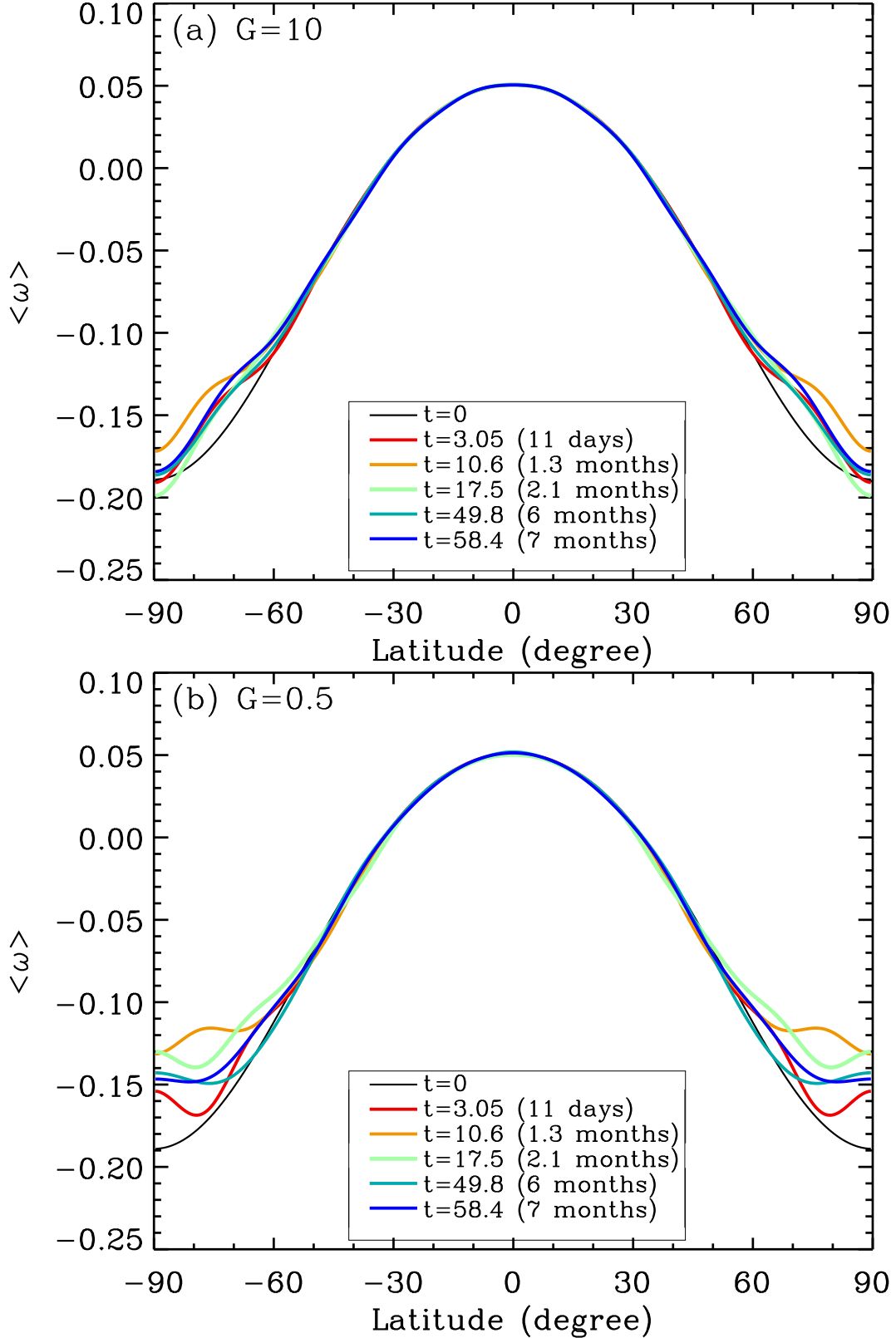


Fig. 4.— Frame (a) shows, for a high effective gravity ( $G = 10$ ) snapshots of longitude-averaged differential rotation at several selected time during the course of its evolution. Frame (b) shows the same, but for a low effective gravity ( $G = 0.5$ ).



We see in Figure 4 that the changes in angular velocity with time are much larger in high than in low latitudes. This is because it is angular momentum that is being transported in latitude by the Reynolds stresses of the perturbations, and the moment of inertia and volume of high latitudes is much smaller than that of low latitudes. So depositing a given amount of angular momentum in high latitudes causes the angular velocity to rise much more there than it falls in low altitudes. It follows that if this instability is active in the solar tachocline, the observed high latitude angular velocity changes would be much larger than those in low latitudes. To date, helioseismic measurements have not been able to tell us whether this is so, because high latitudes are very hard to observe.

For both high and low  $G$ , the peak high latitude angular velocity is reached within a little over one month after the initial disturbance is introduced. Thereafter it fluctuates, but about a distinctly higher polar angular velocity than in the initial state. The polar angular velocity is significantly higher for low  $G$  than high. We reason below that this is because with low  $G$  it is easier for the mass distribution in the shell to be rearranged by meridional flow. The detailed time history of the amplitude of the polar angular velocity does not precisely match the rather smooth oscillation seen in Figure 3. This is not surprising, because the time variation seen in Figure 3 is of global integrals of the energy, while the polar rotation changes are for a very small part of the volume of the global shell.

We can illustrate and explain the physical processes involved in the evolution of the differential rotation by using equations (60)-(62) of Dikpati & Gilman (2001), which we repeat here, rearranged so that only the time derivatives are on the left hand sides.

$$\frac{\partial \overline{u_2}}{\partial t} = F_u - \overline{v_2} \frac{\partial}{\partial \mu} (\omega_0 (1 - \mu^2)), \quad (13)$$

$$\frac{\partial \overline{v_2}}{\partial t} = F_v - 2\omega_0 \overline{u_2} \mu + G\sqrt{1 - \mu^2} \frac{\partial \overline{h_2}}{\partial \mu}, \quad (14)$$

$$\frac{\partial \overline{h_2}}{\partial t} = F_h - \frac{\partial}{\partial \mu} \left( (1 + \overline{h_0}) \overline{v_2} \sqrt{1 - \mu^2} \right), \quad (15)$$

The forcing functions  $F_u$ ,  $F_v$  and  $F_h$  are defined as,

$$\begin{aligned} F_u &= -\overline{v' \frac{\partial}{\partial \mu} (u' \sqrt{1 - \mu^2})}, \\ F_v &= -\overline{\frac{u'}{\sqrt{1 - \mu^2}} \left( \frac{\partial v'}{\partial \lambda} - \sqrt{1 - \mu^2} \frac{\partial}{\partial \mu} (u' \sqrt{1 - \mu^2}) \right)} - \sqrt{1 - \mu^2} \frac{\partial}{\partial \mu} \left( \frac{\overline{u'^2} + \overline{v'^2}}{2} \right), \\ F_h &= -\frac{\partial}{\partial \mu} (\overline{h' v'} \sqrt{1 - \mu^2}). \end{aligned}$$

Here the variables are  $\overline{u_2}$ ,  $\overline{v_2}$  and  $\overline{h_2}$ , which represent respectively the departures of linear rotational velocity, meridional flow, and layer thickness from their initial values.  $\omega_0$  is the angular velocity of the core, and  $\mu$  is cosine of the latitude. From above definitions, one can see that  $F_u$ ,  $F_v$  and  $F_h$  are quadratic functions that contain the covariances or stresses from the perturbation variables  $u, v, h$ . Equations (13) and (14) are, respectively, the equations of motion for differential rotation and meridional flow, and Equation (15) is the mass continuity equation, all for the longitudinal wavenumber  $m = 0$  variables.

Figure 5 displays profiles of layer thickness, meridional flow and angular velocity at the same times as shown in Figure 4b. Thickness (solid purple curve) and latitudinal flow (solid green curve) are shown in frames (a) through (e), along with the initial thickness (dashed purple curve) for reference. Note that initial meridional flow (dashed green curve) is zero. The differential rotation angular velocity (thick black curve) is shown in frames (f)-(j), together with the initial differential rotation (thin curve).

If we compare the thickness and latitudinal flow profiles as time advances, we can see clearly that initially the thickness shrinks near the poles but later rises again as the oscillation progresses. Consistently, the meridional flow is away from the poles while the thickness is declining there, and toward the poles while the polar thickness is rebounding. The same relationship between meridional flow and thickness, dictated by mass conservation, can be seen at all other latitudes. When the polar thickness is declining, the polar angular velocity is increasing.

The physical processes that govern these correlated changes among thickness, meridional flow and differential rotation are contained in Equations (13)-(15) above (see Dikpati & Gilman (2001)). In brief, what happens during the nonlinear oscillation is that, through  $F_u$  (Equation 13) the perturbation Reynolds stress transports angular momentum toward the poles to cause a ‘spin-up’, or higher linear and angular velocity there. In the meridional flow Equation (14), this ‘spin up’ leads to a negative (equatorward) Coriolis force that pushes fluid away from the pole toward the equator. This mass flow then produces a positive latitudinal pressure gradient force, which is expressed as a thickness gradient in a shallow-water model. This force starts to counterbalance the Coriolis force.

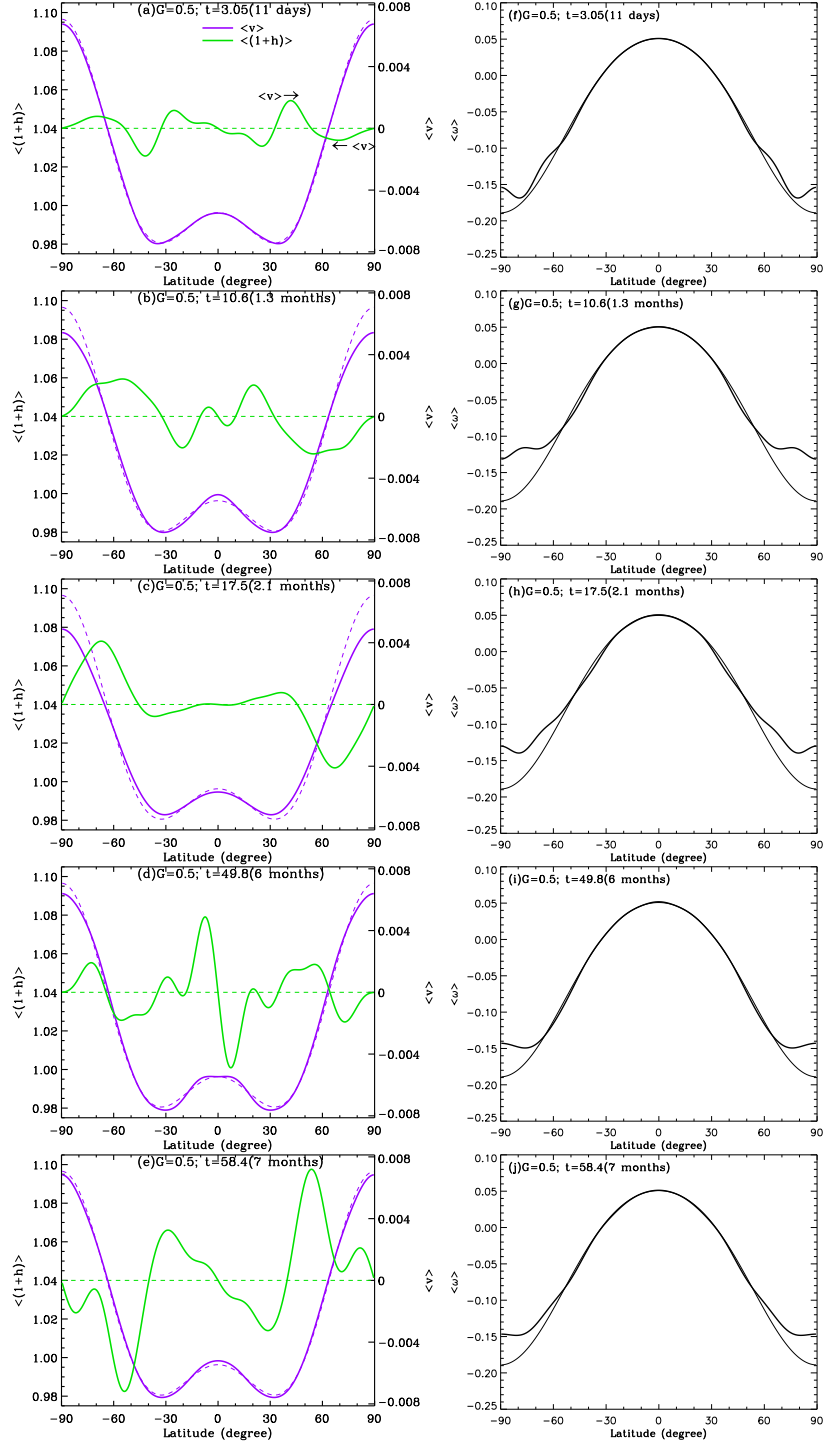


Fig. 5.— Frames (a-e) show, for  $G = 0.5$ , five snapshots of longitude-averaged height deformation (solid purple curves) for the same selected times as in Figure 4(b), and corresponding latitudinal flow (solid green curves) have been superimposed on that. Dashed purple and green curves in each frame respectively present height deformation and latitudinal flow at  $t = 0$ . Solid black curves in frames (f-j) show longitude-averaged differential rotation, for the same selected times, with a superimposed dashed curve for  $t = 0$ . The right column is created by separating five curves of Figure 4b.

This rebalancing of forces will reduce the equatorward meridional flow, but in our nearly dissipation free system, it overshoots, causing the meridional flow to reverse and rebuild the polar thickness. At the same time, the changed differential rotation profile is less unstable to the perturbations, or even stable to them, so the Reynolds stresses get much weaker, and the polar latitudes spin down again. Throughout this sequence of changes, the mass continuity Equation (15) ensures that the changes in thickness are consistent with the changes in meridional flow.

### 3.4. Evolution of disturbance planforms

We can better understand the nonlinear dynamics of the shallow water system by examining the planforms (longitude-latitude) of the flow and thickness as they evolve. Figure 6 displays these quantities for the same times as in Figures 4b and 5 (low  $G$ , 0.5). The left hand column displays the total flow and total thickness fields (blue is thinnest, red thickest); the right hand column shows all of the  $m > 0$  fields, after subtracting out the axisymmetric parts of the differential rotation, meridional flow and axisymmetric thickness.

From both columns we can see that the  $m = 1$  mode dominates in the flow and thickness patterns, leading to a 'meandering' of the E-W flow. As time progresses, more structure and somewhat finer spatial scales develop, as we should expect from the behavior of the energy spectrum shown in Figure 2. We can also see from both columns that the flow is predominantly geostrophic, that is in the North there is counterclockwise circulation around the blue (thinnest) areas, clockwise around the red (thickest) areas; the reverse is true in the South. Since the pressure in the shallow water system is hydrostatic, it is proportional to the thickness, so the counterclockwise flow in the North is around low pressure, the clockwise flow around high pressure.

From the right hand column we can see that in the first 1-2 months the disturbances are transporting angular momentum toward the poles to spin them up, as seen in Figure 4b. The velocity and thickness patterns are tilted with respect to the E-W direction in such a way that the fluid elements moving toward the east in the disturbance are also moving toward the poles, while those moving toward the west (relative to the rotating reference frame) are moving toward the equator. This means there is a correlation between the two velocity components that is the Reynolds stress, which is carrying out the poleward angular momentum transport.

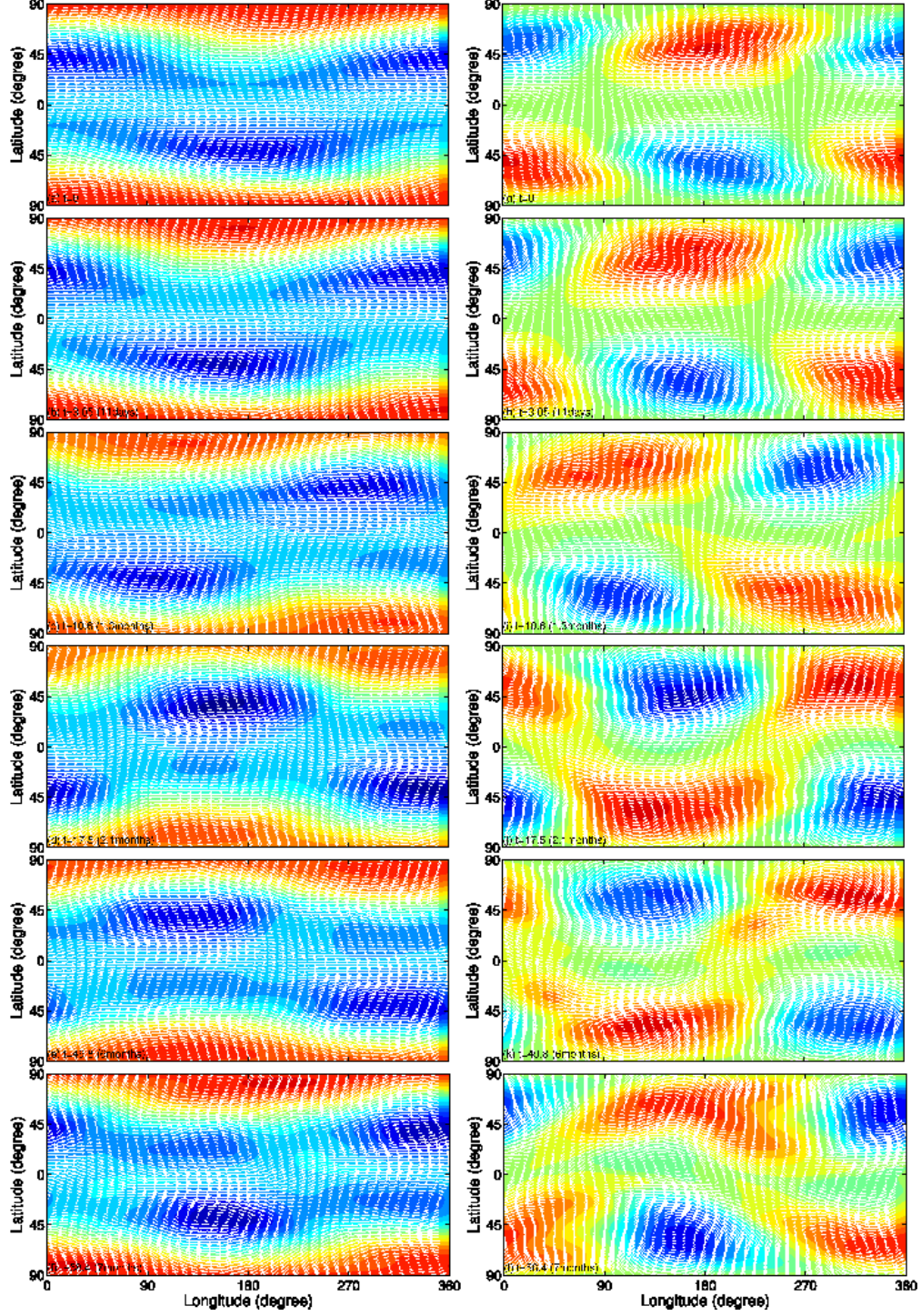


Fig. 6.— Frames (a-f) show, for  $G = 0.5$ , planforms of flow (arrow vector) and height (color map) for five selected times as in Figure 5. Frames (g-l) show the perturbation part of flow and height. Red represents swelling and blue depression.



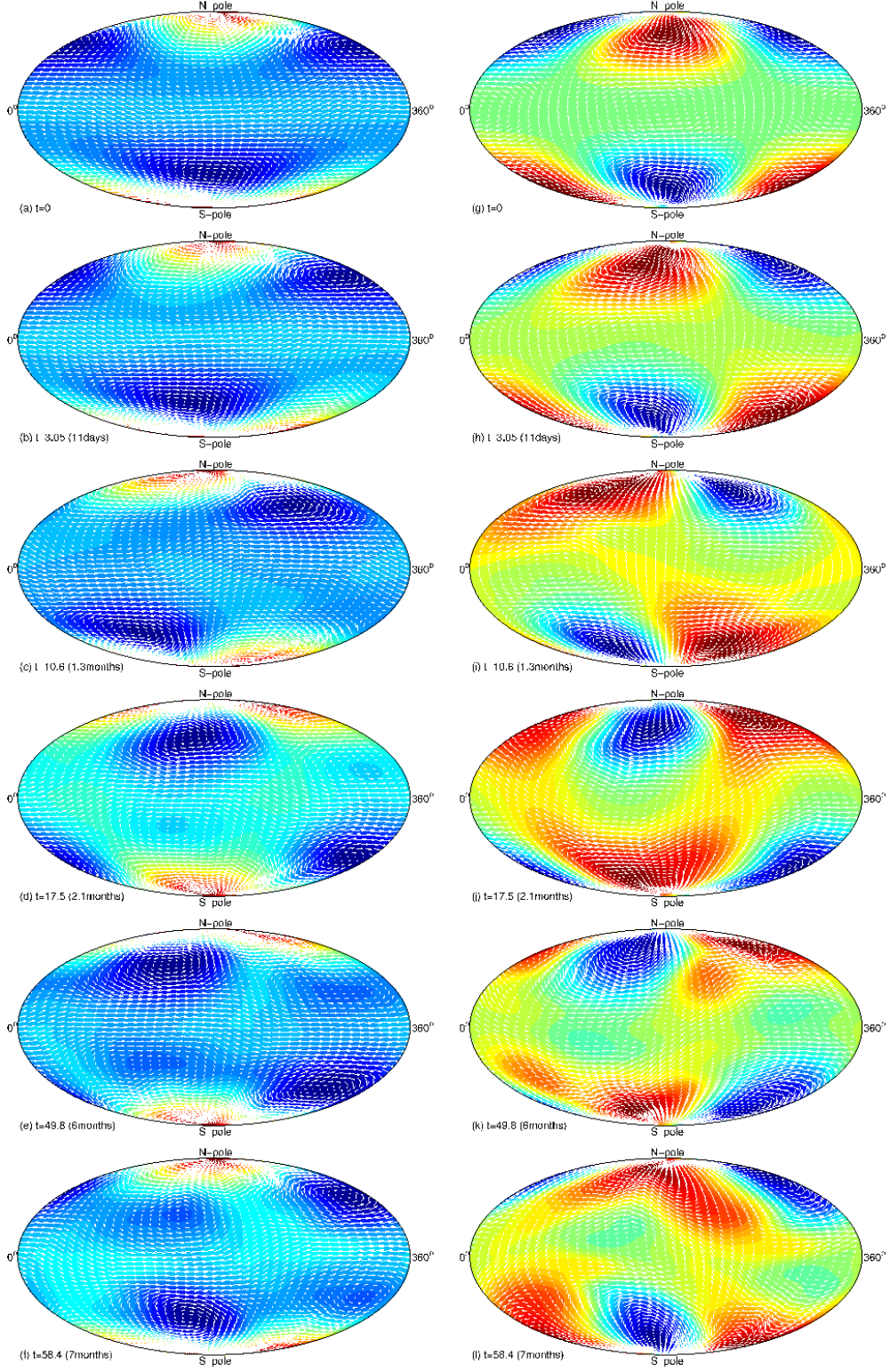


Fig. 7.— Same as in Figure 6, but in Mollweide projection.

By 2.1 months, these tilts are virtually gone, indicating angular momentum is no longer being transported toward the poles. This is consistent with the profiles of differential rotation shown in Figure 4, in which the maximum amount of polar spin-up is reached between 1.3 and 2.1 months in these selected cases. By six months, the perturbation patterns have become more complex, and it is difficult to discern which way the angular momentum transport is going. But from Figure 3 there is still a pronounced amplitude oscillation between the perturbations and the differential rotation and meridional flow. In this nearly dissipation-free system there does not appear to be an absolutely steady nonlinear state. Instead there is a dynamical equilibrium with continuous evolution of all flow patterns within a nonlinear regime in which the high latitude rotation rate, while fluctuating, is almost always faster than in the initial state.

In Figure 7, we repeat the twelve frames (Figure 6a-l) in Mollweide projection. This Figure captures a more realistic look of the global disturbance patterns, particularly at and near the poles. In latitude-longitude plots, the single point at each pole is spread out over  $360^\circ$  longitude. Figure 7 reveals all the features of the disturbances seen in Figure 6, but also reveals more clearly that the flow spreads over both hemispheres crossing the equator.

### 3.5. Is a linearly stable profile nonlinearly unstable?

To illustrate further the range of nonlinear behavior of the shallow water system, we have performed an additional numerical experiment in which we have chosen a combination of differential rotation ( $s = 0.15$ ) and effective gravity ( $G = 10$ ) that we know from linear theory is stable to perturbations, and initially perturbed the system with a disturbance calculated for an unstable case. The amplitude of perturbation used is 20% of the reference state differential rotation. Shown in Figure 8 is the resulting differential rotation evolution sampled at the same times as in previous cases. Here we see that in the first few days of the integration, the disturbance starts to spin up the poles (red curve) because the Reynolds stress in it transports angular momentum toward the poles. But this trend is very short-lived, as the stable differential rotation modifies the disturbance, changing the sign of its Reynolds stress by changing the sense of tilt of the perturbation velocities with respect to the E-W direction. Consequently for the next two months of the integration, the poles actually spin down to lower rotation than they had initially, (light green curve) while the kinetic energy of the differential rotation is increased at the expense of the energy in the disturbance. But this, too, is a transient, and by seven months the rotation at high latitudes has returned to very close to its initial profile (dark blue curve).

The details of how the disturbance evolves with time is shown in Figure 9, which gives

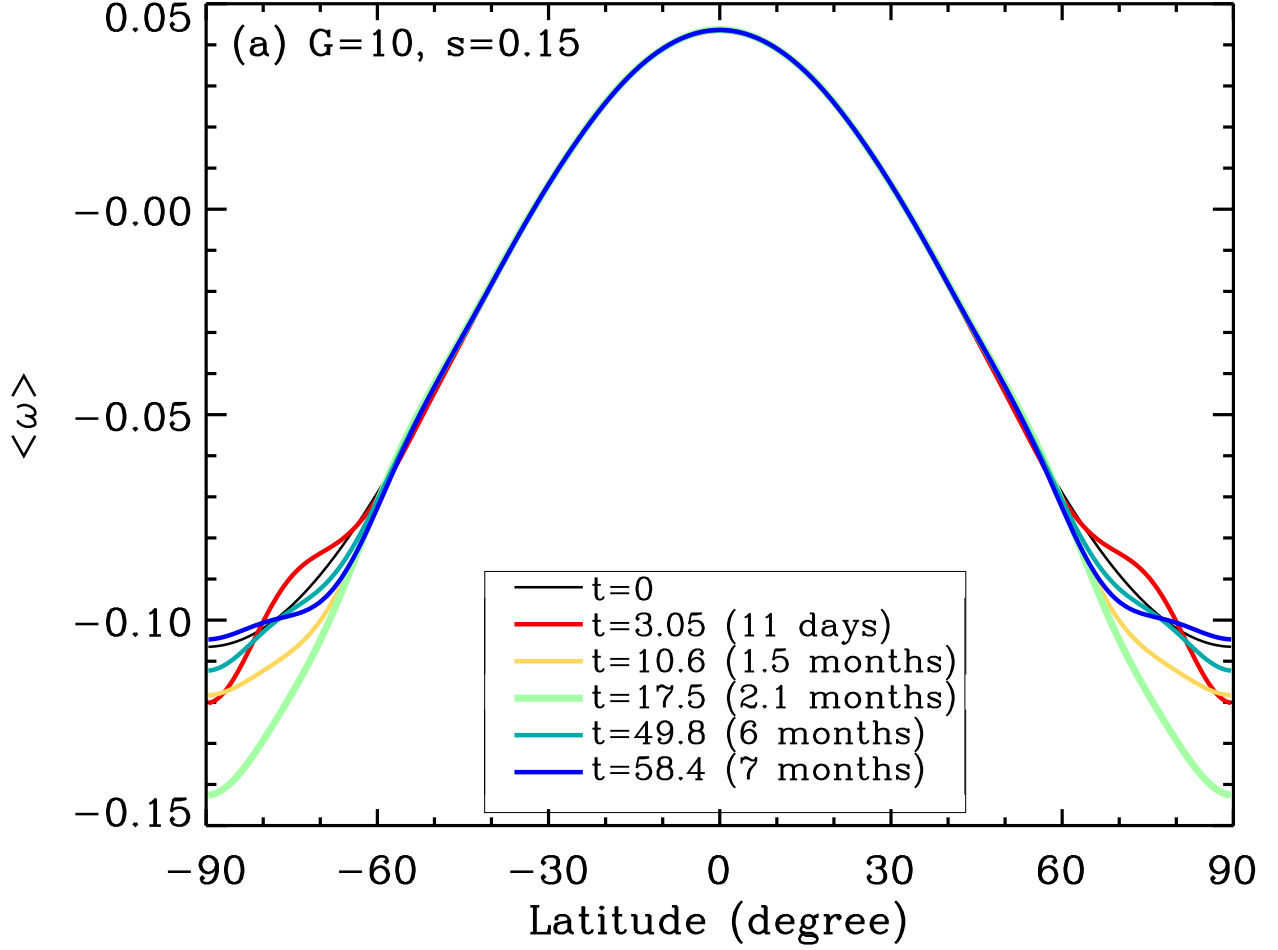


Fig. 8.— Response of a linearly stable solar differential rotation (with  $s = 0.15$  and for  $G = 10$ ) to perturbation. Five snapshots present the evolution of longitude-averaged differential rotation for five selected times as in Figure 5.

longitude-latitude planforms of velocity and shell thickness. The three frames are for, respectively,  $t = 0, 10.6$  and  $49.8$  (0, 1.3 months, and 6 months). We see that in this succession of frames the tilt of the velocity vectors with respect to a latitude circle changes orientation twice, as the associated Reynolds stress changes sign twice, signifying first poleward, then equatorward, then poleward momentum transport again. This is what causes the poles to spin up, then spin down, then up again.



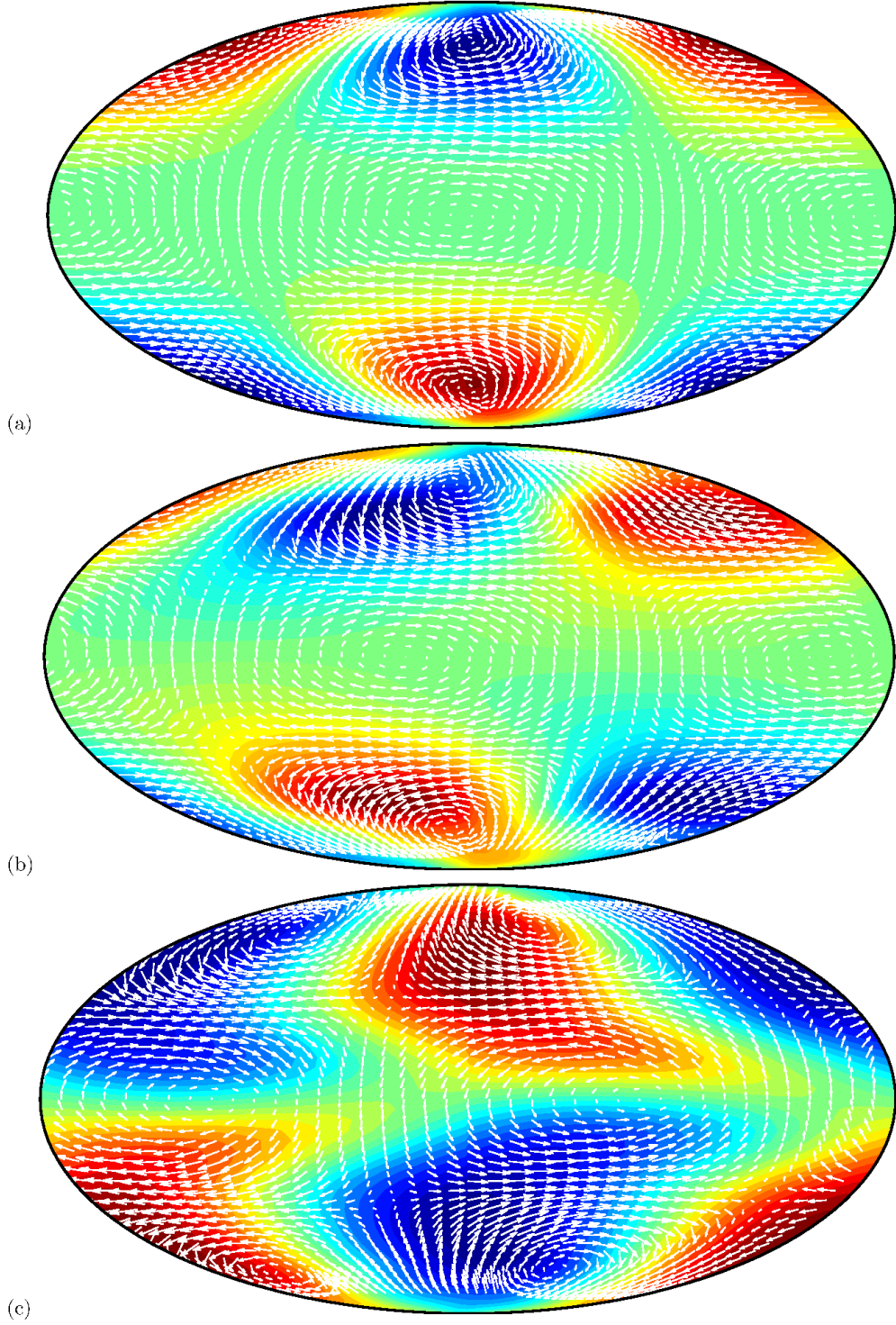


Fig. 9.— Frames (a-c) show, for  $s = 0.15$  and  $G = 10$ , planforms of flow (arrow vector) and height (color map) in Mollweide projection, for three selected times,  $t = 0$ , 1.3 months and 6 months.

Since linear studies (Dikpati & Gilman 2001) indicate that the low differential amplitudes ( $s \lesssim 0.17$ ) are stable in the radiative tachocline with high  $G$ , we considered a case with  $s = 0.15$  and  $G = 10$  in this subsection. In linear studies shallow-water gravity modes were extracted out from the calculation and only shear modes were explored. However, we have no such freedom in the case of nonlinear evolution of a shear profile in the radiative tachocline fluid shell with high  $G$ . Consequently we see the appearance of gravity modes in the evolution discussed in Figures 8 and 9. The generation and evolution of gravity modes is a vast subject of research itself. A forthcoming paper will address the generation of shallow-water gravity modes due to nonadjustment of geostrophic balance when the effective gravity of the system is high.

#### 4. Concluding Comments

We have presented above the first fully nonlinear ‘shallow water’ numerical model to be applied to the Sun. It is intended for use in understanding the global dynamics of solar and stellar tachoclines. It provides a beginning and template for later models that will include global MHD effects; solar tachoclines most likely contain strong global scale magnetic fields, particularly toroidal fields.

This spectral model needs only extremely low numerical diffusion to keep the solutions well behaved, so it is particularly well suited to simulation of strongly nonlinear time dependent hydrodynamics and MHD of the Sun. The equations conserve energy with extremely high accuracy ( $\sim 0.001\%$ ), so that very long simulations are possible without significant spurious build-up of kinetic or potential energy at small scales. Substantial increases in both computational efficiency and accuracy are obtained by use of a mechanism for adjusting the time step during a simulation.

Since the model does include the radial dimension in a simple way, by means of a deforming top surface, it contains gravity wave modes as well as shearing instabilities of the differential rotation. It also allows for a simplified form of meridional flow that is coupled to and causes the changes in the thickness of the spherical shell. Thus it is possible with this model to study rather complex fluid dynamics, including interplay between the relatively low frequency global shearing flows and instabilities, and the higher frequency gravity waves made possible by the deforming top boundary.

The low dissipation in the model is of particular value for simulating the global dynamics of the ‘radiative’ tachocline that is found below the overshooting layer of the convection zone above. But it is equally valuable for simulations applied to the ‘overshoot’ tachocline, whose

differential rotation is maintained by downward diffusion from the convection zone.

Our first results from this nonlinear model focus primarily on the nonlinear interactions between unstable global perturbations previously found from linear analyses and the differential rotation that gives rise to them. We show that the nonlinear dynamics result in a ‘spin-up’ of polar regions due to the Reynolds stress associated with the growing disturbances, and also substantial nonlinear oscillations between disturbance and differential rotation kinetic energy. The oscillation occurs because as the disturbances extract energy and transport momentum to high latitudes, the differential rotation profile changes in such a way as to reduce and even shut off the instability. At least temporarily there can occur a reversal in direction of angular momentum transport, which rebuilds energy in the differential rotation. The simulations go through a sequence of these oscillations without settling to a steady state. This is because the system is virtually dissipation-free due to the implementation of numerical scheme with very little spectral viscosity. Throughout this evolution, the longitude-latitude planform of the disturbances on the differential rotation, as well as the total flow, undergoes considerable evolution as well as propagation in longitude.

The changes in angular velocity with time in polar latitudes are much larger than the compensating changes in low latitudes, because the moment of inertia and volume of polar latitudes is much smaller than in low and mid-latitudes. The period of the nonlinear oscillation is inversely proportional to the amplitude of the initial perturbations, apparently with finite asymptotic periods for both very large and very small initial disturbance energies. Throughout these oscillations the disturbance kinetic energy remains confined primarily to the lowest longitudinal wave numbers,  $m = 1, 2$ , or the largest global scales.

The simulations contain gravity waves of significant amplitude particularly when the effective gravity ( $G$ ) of the system is high; their role will be addressed in a later paper. The solutions also contain kinetic helicity due to the correlation between the local radial component of vorticity and the radial motion associated with changes in the thickness of the shell. Kinetic helicity is of particular importance for the solar dynamo, and will also be studied in more detail in a later paper. In the Sun the differential rotation of the tachocline is imposed from the convection zone above. We will generalize our model to include this forcing in later studies. This will add still another time scale to the problem, namely the time it takes for the top forcing to restore the differential rotation.

All of the additional studies just described are for the hydrodynamic model we have already built. The major step beyond that system is to include global MHD processes, which will without doubt substantially modify the hydrodynamic processes we have studied or will study soon. A still later step will be to couple this model to a global 3D flux transport dynamo model for the Sun, that will be capable of addressing the question of

the origin of active longitudes (Dikpati & Gilman 2005) as well as how such longitudinally dependent features and processes contribute the origin and evolution of solar cycles. The coupling would involve flow generated in the tachocline reaching into the convection zone above and generating 3D MHD induction effects. Thus there is a need to develop a viscous shallow-water model in order to be able to couple the tachocline instabilities with a global, flux-transport dynamo model in the solar convective envelope. In addition, it is necessary for the magnetic fields in the tachocline to connect with that in the convection zone above, continuously through the interface between the tachocline and the convection zone. To implement such a connection among magnetic fields at different layers, through the interfaces among the layers, we would follow the way as described in the figure 1 and equation (22) of Chan, Liao & Zhang (2008).

We thank Phil Judge for reviewing the entire manuscript and for his helpful comments. We extend our thanks to Yuhong Fan for helpful discussions on artificial viscosity in an inviscid model versus viscous model with physical diffusion, to Peter Gilman for many helpful discussions on the topic of this paper, and to an anonymous reviewer for his/her constructive comments and suggestions, which have helped improve this paper. This work is partially supported by NASA’s Living With a Star program through the grant NNX08AQ34G. The National Center for the Atmospheric Research is sponsored by the National Science Foundation.

## 5. Appendix: Solution Technique

In the case of primitive equations such as equations (8)-(10), the vector field (flow) and the scalar field (height) need to be expanded respectively in terms of vector and scalar spherical harmonics, in order to handle the pole problem. Pure scalar harmonics can also be used by converting all the vector fields into scalar fields, but at the expense of raising the order of the equations.

Following the solution method of Swarztrauber (1996) (see method 2 there), the spectral decomposition of scalar  $h$  can be expressed as

$$h(\phi, \lambda) = \sum_{l=0}^N \sum_{m=0}^l P_{lm} (a_r^{lm} \cos m\lambda + a_i^{lm} \sin m\lambda), \quad (A1)$$

where

$$\sqrt{\alpha_{lm}} = \frac{2l+1}{2\pi} \frac{(l-m)!}{(l+m)!}, \quad (A2)$$

and  $P_{lm}$  is the Associated Legendre polynomial of order  $(l, m)$ . The  $\star$  in the  $m$  summation implies a factor of  $\frac{1}{2}$  is multiplied when  $m$  equals 0. The coefficients  $a_r^{lm}$  and  $a_i^{lm}$  can be obtained from the inverse transform as

$$a_r^{lm} = \int_{-\frac{\pi}{2}}^{\frac{\pi}{2}} d\phi P_{lm}(\phi) \cos \phi \int_0^{2\pi} d\lambda \cos m\lambda h(\phi, \lambda), \quad (A3)$$

$$a_i^{lm} = \int_{-\frac{\pi}{2}}^{\frac{\pi}{2}} d\phi P_{lm}(\phi) \cos \phi \int_0^{2\pi} d\lambda \sin m\lambda h(\phi, \lambda). \quad (A4)$$

In order to express the vector fields ( $u$  and  $v$ ), we define the vector spherical harmonic components as

$$\sqrt{l(l+1)}V_{lm}(\phi) = \frac{dP_{lm}}{d\phi} = \frac{1}{2} \{ (l+m)(l-m+1)P_{l(m-1)} - P_{l(m+1)} \}, \quad (A5)$$

$$\sqrt{l(l+1)}W_{lm}(\phi) = \frac{mP_{lm}}{\cos \phi} = \frac{(-1)}{2} \{ P_{(l-1)(m+1)} + (l+m)(l+m-1)P_{(l-1)(m-1)} \}. \quad (A6)$$

The unit vectors can be constructed as

$$B_{lm} = \begin{pmatrix} iW_{lm} \\ V_{lm} \end{pmatrix} e^{im\lambda}, \quad C_{lm} = \begin{pmatrix} -V_{lm} \\ iW_{lm} \end{pmatrix} e^{im\lambda} \quad (A7)$$

It is easy to check that  $B_{lm}$  and  $C_{lm}$  satisfy the following orthogonality relations

$$(B_{ij}, C_{lm}) = 0, \quad (A8a)$$

$$(B_{ij}, B_{lm}) = (C_{ij}, C_{lm}) = \alpha_{lm} \cdot \delta_{il} \cdot \delta_{jm}, \quad (A8b)$$

in which  $\delta_{ij}$  is Krönecker- $\delta$ . The velocity components can now be expressed in terms of vector spherical harmonics as

$$\begin{aligned} u(\phi, \lambda) = & \sum_{l=0}^N \sum_{m=0}^{l'} \{ W_{lm} (b_i^{lm} \cos m\lambda - b_r^{lm} \sin m\lambda) \\ & + V_{lm} (c_r^{lm} \cos m\lambda + c_i^{lm} \sin m\lambda) \}, \end{aligned} \quad (A9)$$

$$v(\phi, \lambda) = \sum_{l=0}^N \sum_{m=0}^{l'} \left\{ V_{lm} (b_r^{lm} \cos m\lambda + b_i^{lm} \sin m\lambda) + W_{lm} (-c_i^{lm} \cos m\lambda + c_r^{lm} \sin m\lambda) \right\}. \quad (A10)$$

The coefficients,  $b_r^{lm}, b_i^{lm}, c_r^{lm}, c_i^{lm}$ , can be evaluated using the following inverse transforms:

$$b_r^{lm} = \frac{1}{\sqrt{\alpha_{lm}}} \left\{ \int_{-\frac{\pi}{2}}^{\frac{\pi}{2}} d\phi \cos \phi V_{lm} \int_0^{2\pi} d\lambda v \cos m\lambda - \int_{-\frac{\pi}{2}}^{\frac{\pi}{2}} d\phi \cos \phi W_{lm} \int_0^{2\pi} d\lambda u \sin m\lambda \right\}, \quad (A11)$$

$$b_i^{lm} = \frac{1}{\sqrt{\alpha_{lm}}} \left\{ \int_{-\frac{\pi}{2}}^{\frac{\pi}{2}} d\phi \cos \phi W_{lm} \int_0^{2\pi} d\lambda u \cos m\lambda + \int_{-\frac{\pi}{2}}^{\frac{\pi}{2}} d\phi \cos \phi V_{lm} \int_0^{2\pi} d\lambda v \sin m\lambda \right\}, \quad (A12)$$

$$c_r^{lm} = \frac{1}{\sqrt{\alpha_{lm}}} \left\{ \int_{-\frac{\pi}{2}}^{\frac{\pi}{2}} d\phi \cos \phi V_{nm} \int_0^{2\pi} d\lambda u \cos m\lambda + \int_{-\frac{\pi}{2}}^{\frac{\pi}{2}} d\phi \cos \phi W_{lm} \int_0^{2\pi} d\lambda v \sin m\lambda \right\}, \quad (A13)$$

$$c_i^{lm} = -\frac{1}{\sqrt{\alpha_{lm}}} \left\{ \int_{-\frac{\pi}{2}}^{\frac{\pi}{2}} d\phi \cos \phi W_{lm} \int_0^{2\pi} d\lambda v \cos m\lambda + \int_{-\frac{\pi}{2}}^{\frac{\pi}{2}} d\phi \cos \phi V_{lm} \int_0^{2\pi} d\lambda u \sin m\lambda \right\}. \quad (A14)$$

Substituting (A9-A14) in equations (7a) and (7b) and performing a few steps of algebra (see equations A.14 and A.15 of Swarztrauber (1996) for detailed derivation), we can obtain the following expressions for the variables  $\zeta$  and  $\delta$ , which no longer contain the unbounded terms that cause the pole problem in spherical polar coordinate system:

$$\zeta = \sum_{l=0}^N \sum_{m=0}^{l'} \sqrt{l(l+1)} P_{lm} (c_r^{lm} \cos m\lambda + c_i^{lm} \sin m\lambda), \quad (A15)$$

$$\delta = \sum_{l=0}^N \sum_{m=0}^{l'} \sqrt{l(l+1)} P_{lm} (b_r^{lm} \cos m\lambda + b_i^{lm} \sin m\lambda). \quad (A16)$$

Similarly following Swarztrauber (1996) (see his equations A.16 and A.17) the expression for the gradient of the scalar variable,  $h$ , can be given as

$$\frac{1}{\cos \phi} \frac{\partial h}{\partial \lambda} = \sum_{l=0}^N \sum_{m=0}^l \sqrt{l(l+1)} W_{lm} (a_i^{lm} \cos m\lambda - a_r^{lm} \sin m\lambda), \quad (A17)$$

$$\frac{\partial h}{\partial \phi} = \sum_{l=0}^N \sum_{m=0}^l \sqrt{l(l+1)} V_{lm} (a_r^{lm} \cos m\lambda + a_i^{lm} \sin m\lambda). \quad (A18)$$

By grouping the derivative and algebraic terms and using the compact notations, defined as

$$\Xi_u = (\zeta + 2\omega_c \sin \phi)v, \quad (A19)$$

$$\Xi_v = -(\zeta + 2\omega_c \sin \phi)u, \quad (A20)$$

the time-evolution equations for  $u$  and  $v$  can be written as

$$\frac{\partial u}{\partial t} = \Xi_u - \frac{1}{\cos \phi} \frac{\partial}{\partial \lambda} \left[ \left( \frac{u^2 + v^2}{2} \right) + Gh \right], \quad (A21)$$

$$\frac{\partial v}{\partial t} = \Xi_v - \frac{\partial}{\partial \phi} \left[ \left( \frac{u^2 + v^2}{2} \right) + Gh \right]. \quad (A22)$$

Note that  $\Xi_u$  and  $\Xi_v$  can be expressed in terms of  $V_{lm}$  and  $W_{lm}$  in an analogous way as  $u$  and  $v$  have been expressed in the Equations A9 and A10.

In order to derive the time-evolution equations for  $u$  and  $v$  in spectral space we differentiate equations (A11-A14) with respect to time and obtain the following:

$$\frac{\partial b_r^{lm}}{\partial t} = \frac{1}{\sqrt{\alpha_{lm}}} \left[ \int_{-\frac{\pi}{2}}^{\frac{\pi}{2}} d\phi \cos \phi V_{lm} \int_0^{2\pi} d\lambda \cos m\lambda \cdot \dot{v} - \int_{-\frac{\pi}{2}}^{\frac{\pi}{2}} d\phi \cos \phi W_{lm} \int_0^{2\pi} d\lambda \sin m\lambda \cdot \dot{u} \right], \quad (A23)$$

$$\frac{\partial b_i^{lm}}{\partial t} = \frac{1}{\sqrt{\alpha_{lm}}} \left[ \int_{-\frac{\pi}{2}}^{\frac{\pi}{2}} d\phi \cos \phi W_{lm} \int_0^{2\pi} d\lambda \cos m\lambda \cdot \dot{u} + \int_{-\frac{\pi}{2}}^{\frac{\pi}{2}} d\phi \cos \phi V_{lm} \int_0^{2\pi} d\lambda \sin m\lambda \cdot \dot{v} \right], \quad (A24)$$

$$\frac{\partial c_r^{lm}}{\partial t} = \frac{1}{\sqrt{\alpha_{lm}}} \left[ \int_{-\frac{\pi}{2}}^{\frac{\pi}{2}} d\phi \cos \phi V_{lm} \int_0^{2\pi} d\lambda \cos m\lambda \cdot \dot{u} + \int_{-\frac{\pi}{2}}^{\frac{\pi}{2}} d\phi \cos \phi W_{lm} \int_0^{2\pi} d\lambda \sin m\lambda \cdot \dot{v} \right], \quad (A25)$$

$$\frac{\partial c_i^{lm}}{\partial t} = -\frac{1}{\sqrt{\alpha_{lm}}} \left[ \int_{-\frac{\pi}{2}}^{\frac{\pi}{2}} d\phi \cos \phi W_{lm} \int_0^{2\pi} d\lambda \cos m\lambda \cdot \dot{v} + \int_{-\frac{\pi}{2}}^{\frac{\pi}{2}} d\phi \cos \phi V_{lm} \int_0^{2\pi} d\lambda \sin m\lambda \cdot \dot{u} \right], \quad (A26)$$

in which,  $\dot{u}$  and  $\dot{v}$  respectively denote the time derivatives of  $u$  and  $v$ . Substituting  $\dot{u}$  and  $\dot{v}$  from equations (A21) and (A22) in the above equations (A23-A26), we obtain

$$\begin{aligned} \frac{\partial b_r^{lm}}{\partial t} &= \frac{1}{\sqrt{\alpha_{lm}}} \left\{ \int_{-\frac{\pi}{2}}^{\frac{\pi}{2}} d\phi \cos \phi V_{lm} \int_0^{2\pi} d\lambda \Xi_v \cos m\lambda - \int_{-\frac{\pi}{2}}^{\frac{\pi}{2}} d\phi \cos \phi W_{lm} \int_0^{2\pi} d\lambda \Xi_u \sin m\lambda \right\} \\ &\quad - \frac{1}{\sqrt{\alpha_{lm}}} \left[ \int_{-\frac{\pi}{2}}^{\frac{\pi}{2}} d\phi \cos \phi V_{lm} \int_0^{2\pi} d\lambda \cos m\lambda \cdot \frac{\partial}{\partial \phi} \left( \frac{u^2 + v^2}{2} + Gh \right) \right. \\ &\quad \left. - \int_{-\frac{\pi}{2}}^{\frac{\pi}{2}} d\phi \cos \phi W_{lm} \int_0^{2\pi} d\lambda \sin m\lambda \cdot \frac{1}{\cos \phi} \frac{\partial}{\partial \lambda} \left( \frac{u^2 + v^2}{2} + Gh \right) \right], \\ &= b_r^{lm}(\Xi) - \frac{1}{\sqrt{\alpha_{lm}}} \left[ \int_{-\frac{\pi}{2}}^{\frac{\pi}{2}} d\phi \cos \phi V_{lm} \int_0^{2\pi} d\lambda \cos m\lambda \cdot \frac{\partial}{\partial \phi} \left( \frac{u^2 + v^2}{2} + Gh \right) \right. \\ &\quad \left. - \int_{-\frac{\pi}{2}}^{\frac{\pi}{2}} d\phi \cos \phi W_{lm} \int_0^{2\pi} d\lambda \sin m\lambda \cdot \frac{1}{\cos \phi} \frac{\partial}{\partial \lambda} \left( \frac{u^2 + v^2}{2} + Gh \right) \right], \quad (A27) \end{aligned}$$

$$\begin{aligned} \frac{\partial b_i^{lm}}{\partial t} &= \frac{1}{\sqrt{\alpha_{lm}}} \left\{ \int_{-\frac{\pi}{2}}^{\frac{\pi}{2}} d\phi \cos \phi W_{lm} \int_0^{2\pi} d\lambda \Xi_u \cos m\lambda + \int_{-\frac{\pi}{2}}^{\frac{\pi}{2}} d\phi \cos \phi V_{lm} \int_0^{2\pi} d\lambda \Xi_v \sin m\lambda \right\} \\ &\quad - \frac{1}{\sqrt{\alpha_{lm}}} \left[ \int_{-\frac{\pi}{2}}^{\frac{\pi}{2}} d\phi \cos \phi W_{lm} \int_0^{2\pi} d\lambda \cos m\lambda \cdot \frac{1}{\cos \phi} \frac{\partial}{\partial \lambda} \left( \frac{u^2 + v^2}{2} + Gh \right) \right. \\ &\quad \left. + \int_{-\frac{\pi}{2}}^{\frac{\pi}{2}} d\phi \cos \phi V_{lm} \int_0^{2\pi} d\lambda \sin m\lambda \cdot \frac{\partial}{\partial \phi} \left( \frac{u^2 + v^2}{2} + Gh \right) \right], \end{aligned}$$



$$\begin{aligned}
&= b_i^{lm}(\Xi) - \frac{1}{\sqrt{\alpha_{lm}}} \left[ \int_{-\frac{\pi}{2}}^{\frac{\pi}{2}} d\phi \cos \phi W_{lm} \int_0^{2\pi} d\lambda \cos m\lambda \cdot \frac{1}{\cos \phi} \frac{\partial}{\partial \lambda} \left( \frac{u^2 + v^2}{2} + Gh \right) \right. \\
&\quad \left. + \int_{-\frac{\pi}{2}}^{\frac{\pi}{2}} d\phi \cos \phi V_{lm} \int_0^{2\pi} d\lambda \sin m\lambda \cdot \frac{\partial}{\partial \phi} \left( \frac{u^2 + v^2}{2} + Gh \right) \right], \tag{A28}
\end{aligned}$$

$$\begin{aligned}
\frac{\partial c_r^{lm}}{\partial t} &= \frac{1}{\sqrt{\alpha_{lm}}} \left\{ \int_{-\frac{\pi}{2}}^{\frac{\pi}{2}} d\phi \cos \phi V_{nm} \int_0^{2\pi} d\lambda \Xi_u \cos m\lambda + \int_{-\frac{\pi}{2}}^{\frac{\pi}{2}} d\phi \cos \phi W_{lm} \int_0^{2\pi} d\lambda \Xi_v \sin m\lambda \right\} \\
&\quad - \frac{1}{\sqrt{\alpha_{lm}}} \left[ \int_{-\frac{\pi}{2}}^{\frac{\pi}{2}} d\phi \cos \phi V_{lm} \int_0^{2\pi} d\lambda \cos m\lambda \cdot \frac{1}{\cos \phi} \frac{\partial}{\partial \lambda} \left( \frac{u^2 + v^2}{2} + Gh \right) \right. \\
&\quad \left. + \int_{-\frac{\pi}{2}}^{\frac{\pi}{2}} d\phi \cos \phi W_{lm} \int_0^{2\pi} d\lambda \sin m\lambda \cdot \frac{\partial}{\partial \phi} \left( \frac{u^2 + v^2}{2} + Gh \right) \right], \\
&= c_r^{lm}(\Xi) - \frac{1}{\sqrt{\alpha_{lm}}} \left[ \int_{-\frac{\pi}{2}}^{\frac{\pi}{2}} d\phi \cos \phi V_{lm} \int_0^{2\pi} d\lambda \cos m\lambda \cdot \frac{1}{\cos \phi} \frac{\partial}{\partial \lambda} \left( \frac{u^2 + v^2}{2} + Gh \right) \right. \\
&\quad \left. + \int_{-\frac{\pi}{2}}^{\frac{\pi}{2}} d\phi \cos \phi W_{lm} \int_0^{2\pi} d\lambda \sin m\lambda \cdot \frac{\partial}{\partial \phi} \left( \frac{u^2 + v^2}{2} + Gh \right) \right], \tag{A29}
\end{aligned}$$

$$\begin{aligned}
\frac{\partial c_i^{lm}}{\partial t} &= -\frac{1}{\sqrt{\alpha_{lm}}} \left\{ \int_{-\frac{\pi}{2}}^{\frac{\pi}{2}} d\phi \cos \phi W_{lm} \int_0^{2\pi} d\lambda \Xi_v \cos m\lambda + \int_{-\frac{\pi}{2}}^{\frac{\pi}{2}} d\phi \cos \phi V_{lm} \int_0^{2\pi} d\lambda \Xi_u \sin m\lambda \right\} \\
&\quad - \frac{1}{\sqrt{\alpha_{lm}}} \left[ \int_{-\frac{\pi}{2}}^{\frac{\pi}{2}} d\phi \cos \phi W_{lm} \int_0^{2\pi} d\lambda \cos m\lambda \cdot \frac{\partial}{\partial \phi} \left( \frac{u^2 + v^2}{2} + Gh \right) \right. \\
&\quad \left. - \int_{-\frac{\pi}{2}}^{\frac{\pi}{2}} d\phi \cos \phi V_{lm} \int_0^{2\pi} d\lambda \sin m\lambda \cdot \frac{1}{\cos \phi} \frac{\partial}{\partial \lambda} \left( \frac{u^2 + v^2}{2} + Gh \right) \right]. \\
&= c_i^{lm}(\Xi) - \frac{1}{\sqrt{\alpha_{lm}}} \left[ \int_{-\frac{\pi}{2}}^{\frac{\pi}{2}} d\phi \cos \phi W_{lm} \int_0^{2\pi} d\lambda \cos m\lambda \cdot \frac{\partial}{\partial \phi} \left( \frac{u^2 + v^2}{2} + Gh \right) \right. \\
&\quad \left. - \int_{-\frac{\pi}{2}}^{\frac{\pi}{2}} d\phi \cos \phi V_{lm} \int_0^{2\pi} d\lambda \sin m\lambda \cdot \frac{1}{\cos \phi} \frac{\partial}{\partial \lambda} \left( \frac{u^2 + v^2}{2} + Gh \right) \right]. \tag{A30}
\end{aligned}$$

As in the case of the meteorological primitive equations, the shallow water equations in the solar case admit high frequency gravity waves as well as low frequency shearing flows.

In order to increase the efficiency of the computation, we employ an implicit scheme for the linear terms and an explicit scheme for the nonlinear terms of the Equations (A27-A30). Therefore we sort out those terms and represent them in their corresponding spectral forms.

Starting with the Equation (A27), we have the following linear term:

$$-\frac{1}{\sqrt{\alpha_{lm}}} \left[ \int_{-\frac{\pi}{2}}^{\frac{\pi}{2}} d\phi \cos \phi V_{lm} \int_0^{2\pi} d\lambda \cos m\lambda \left( G \frac{\partial h}{\partial \phi} \right) - \int_{-\frac{\pi}{2}}^{\frac{\pi}{2}} d\phi \cos \phi W_{lm} \int_0^{2\pi} d\lambda \sin m\lambda \left( G \frac{1}{\cos \phi} \frac{\partial h}{\partial \lambda} \right) \right].$$

Substituting the expressions for  $\frac{1}{\cos \phi} \frac{\partial h}{\partial \lambda}$  and  $\frac{\partial h}{\partial \phi}$  from Equations (A17) and (A18) into the above expression, and applying the orthogonality relation from Equation (A7), we obtain

$$\begin{aligned} & -\frac{1}{\sqrt{\alpha_{lm}}} \left[ \int_{-\frac{\pi}{2}}^{\frac{\pi}{2}} d\phi \cos \phi V_{lm} \int_0^{2\pi} d\lambda \cos m\lambda \sum_{l_1=0}^N \sum_{m_1=0}^{l_1} \sqrt{l_1(l_1+1)} G V_{l_1 m_1} (a_r^{l_1 m_1} \cos m_1 \lambda + a_i^{l_1 m_1} \sin m_1 \lambda) \right. \\ & \left. - \int_{-\frac{\pi}{2}}^{\frac{\pi}{2}} d\phi \cos \phi W_{lm} \int_0^{2\pi} d\lambda \sin m\lambda \sum_{l_1=0}^N \sum_{m_1=0}^{l_1} \sqrt{(l_1+1)} G W_{l_1 m_1} \cdot (a_i^{l_1 m_1} \cos m_1 \lambda - a_r^{l_1 m_1} \sin m_1 \lambda) \right] \\ & = -\frac{\pi}{\sqrt{\alpha_{lm}}} \sum_{l_1=0}^N \sum_{m_1=0}^{l_1} a_r^{l_1 m_1} \sqrt{l_1(l_1+1)} \int_{-\frac{\pi}{2}}^{\frac{\pi}{2}} d\phi \cos \phi \cdot G (V_{lm} V_{l_1 m_1} + W_{lm} W_{l_1 m_1}) \\ & = -a_r^{lm} G \sqrt{l(l+1)}. \end{aligned} \tag{A31}$$

A part of the nonlinear terms of equation (A27) contains the derivative of  $(u^2 + v^2)/2$ . Noting that  $(u^2 + v^2)/2$  is a scalar term which is represented in spectral space as

$$\frac{u^2 + v^2}{2} = \sum_{l=0}^N \sum_{m=0}^l P_{lm} (d_r^{lm} \cos m\lambda + d_i^{lm} \sin m\lambda), \tag{A32}$$

we can use similar formulae as given in expressions (A17) and (A18) for the derivative of a scalar variable to evaluate the derivatives of  $(u^2 + v^2)/2$ . After a few steps of algebra, those terms can be simplified to

$$\begin{aligned} & - \left[ \int_{-\frac{\pi}{2}}^{\frac{\pi}{2}} d\phi \cos \phi V_{lm} \int_0^{2\pi} d\lambda \cos m\lambda \cdot \frac{\partial}{\partial \phi} \left( \frac{u^2 + v^2}{2} \right) \right. \\ & \left. - \int_{-\frac{\pi}{2}}^{\frac{\pi}{2}} d\phi \cos \phi W_{lm} \int_0^{2\pi} d\lambda \sin m\lambda \cdot \frac{1}{\cos \phi} \frac{\partial}{\partial \lambda} \left( \frac{u^2 + v^2}{2} \right) \right] \\ & = - (G \cdot a_r^{lm} + d_r^{lm}) \sqrt{l(l+1)}. \end{aligned}$$

Performing similar analysis for the nonlinear terms involving derivatives of  $(u^2 + v^2)/2$  respectively in equations (A28-A30), we get

$$\begin{aligned}
& - \left[ \int_{-\frac{\pi}{2}}^{\frac{\pi}{2}} d\phi \cos \phi W_{lm} \int_0^{2\pi} d\lambda \cos m\lambda \cdot \frac{1}{\cos \phi} \frac{\partial}{\partial \lambda} \left( \frac{u^2 + v^2}{2} \right) \right. \\
& \quad \left. + \int_{-\frac{\pi}{2}}^{\frac{\pi}{2}} d\phi \cos \phi V_{lm} \int_0^{2\pi} d\lambda \sin m\lambda \cdot \frac{\partial}{\partial \phi} \left( \frac{u^2 + v^2}{2} \right) \right] \\
& \quad = - (g \cdot a_i^{lm} + d_i^{lm}) \sqrt{l(l+1)}, \\
& - \left[ \int_{-\frac{\pi}{2}}^{\frac{\pi}{2}} d\phi \cos \phi V_{lm} \int_0^{2\pi} d\lambda \cos m\lambda \cdot \frac{1}{\cos \phi} \frac{\partial}{\partial \lambda} \left( \frac{u^2 + v^2}{2} \right) \right. \\
& \quad \left. + \int_{-\frac{\pi}{2}}^{\frac{\pi}{2}} d\phi \cos \phi W_{lm} \int_0^{2\pi} d\lambda \sin m\lambda \cdot \frac{\partial}{\partial \phi} \left( \frac{u^2 + v^2}{2} \right) \right] = 0, \\
& - \left[ \int_{-\frac{\pi}{2}}^{\frac{\pi}{2}} d\phi \cos \phi W_{lm} \int_0^{2\pi} d\lambda \cos m\lambda \cdot \frac{\partial}{\partial \phi} \left( \frac{u^2 + v^2}{2} \right) \right. \\
& \quad \left. - \int_{-\frac{\pi}{2}}^{\frac{\pi}{2}} d\phi \cos \phi V_{lm} \int_0^{2\pi} d\lambda \sin m\lambda \cdot \frac{1}{\cos \phi} \frac{\partial}{\partial \lambda} \left( \frac{u^2 + v^2}{2} \right) \right] = 0.
\end{aligned}$$

Recalling Equation (3) from §2.1, we now write it as

$$\frac{\partial h}{\partial t} = \Psi - \delta, \quad (A33),$$

in which

$$\Psi = -h\delta - \frac{u}{\cos \phi} \frac{\partial h}{\partial \lambda} - v \frac{\partial h}{\partial \phi}. \quad (A34)$$

To obtain the time-evolution equations for the spectral coefficients involved in  $h$ , we differentiate Equations (A3) and (A4) with respect to time and using equation (A33) we obtain

$$\begin{aligned}
\frac{\partial a_r^{lm}}{\partial t} &= \frac{1}{\sqrt{\alpha_{lm}}} \int_{-\frac{\pi}{2}}^{\frac{\pi}{2}} d\phi P_{lm}(\phi) \cos \phi \int_0^{2\pi} d\lambda \cos m\lambda \cdot \Psi \\
& - \frac{1}{\sqrt{\alpha_{lm}}} \int_{-\frac{\pi}{2}}^{\frac{\pi}{2}} d\phi P_{lm}(\phi) \cos \phi \int_0^{2\pi} d\lambda \cos m\lambda \cdot \delta,
\end{aligned} \quad (A35)$$

$$\begin{aligned}\frac{\partial a_i^{lm}}{\partial t} &= \frac{1}{\sqrt{\alpha_{lm}}} \int_{-\frac{\pi}{2}}^{\frac{\pi}{2}} d\phi P_{lm}(\phi) \cos \phi \int_0^{2\pi} d\lambda \sin m\lambda \cdot \Psi(\phi, \lambda) \\ &\quad - \frac{1}{\sqrt{\alpha_{lm}}} \int_{-\frac{\pi}{2}}^{\frac{\pi}{2}} d\phi P_{lm}(\phi) \cos \phi \int_0^{2\pi} d\lambda \sin m\lambda \cdot \delta.\end{aligned}\tag{A36}$$

Substituting in equations (A35) and (A36), the expression for  $\delta$  from equation (A16), and using orthogonality of Legendre polynomials we get

$$\begin{aligned}\frac{\partial a_r^{lm}}{\partial t} &= \frac{1}{\sqrt{\alpha_{lm}}} \int_{-\frac{\pi}{2}}^{\frac{\pi}{2}} d\phi P_{lm}(\phi) \cos \phi \int_0^{2\pi} d\lambda \cos m\lambda \cdot \Psi + \sqrt{l(l+1)} b_r^{lm}, \\ &= a_r^{lm}(\Psi) + \sqrt{l(l+1)} b_r^{lm},\end{aligned}\tag{A37}$$

$$\begin{aligned}\frac{\partial a_i^{lm}}{\partial t} &= \frac{1}{\sqrt{\alpha_{lm}}} \int_{-\frac{\pi}{2}}^{\frac{\pi}{2}} d\phi P_{lm}(\phi) \cos \phi \int_0^{2\pi} d\lambda \sin m\lambda \cdot \Psi(\phi, \lambda) + \sqrt{l(l+1)} b_i^{lm}. \\ &= a_i^{lm}(\Psi) + \sqrt{l(l+1)} b_i^{lm},\end{aligned}\tag{A38}$$

The Equations (A27-A30) and (A37-A38) represent the full set of hydrodynamic shallow-water Equations (1-3) of §2.1 in the spectral form. Like the Equations (A37) and (A38), the Equations (A27-A30) can also be expressed in compact form as

$$\frac{\partial b_r^{lm}}{\partial t} = b_r^{lm}(\Xi) - \sqrt{l(l+1)} d_r^{lm} - G \sqrt{l(l+1)} a_r^{lm},\tag{A39}$$

$$\frac{\partial b_i^{lm}}{\partial t} = b_i^{lm}(\Xi) - \sqrt{l(l+1)} d_i^{lm} - G \sqrt{l(l+1)} a_i^{lm},\tag{A40}$$

$$\frac{\partial c_r^{lm}}{\partial t} = c_r^{lm}(\Xi).\tag{A41}$$

Note that due to certain symmetry properties (antisymmetry here) of  $V_{lm}$  and  $W_{lm}$ , 2nd and 3rd terms in the right hand side of  $\frac{\partial c_r^{lm}}{\partial t}$  equation (Equation (29)) get cancelled. Similar cancellation happens also in Equation (30) for  $\frac{\partial c_i^{lm}}{\partial t}$ , which is reproduced in compact form below, namely

$$\frac{\partial c_i^{lm}}{\partial t} = c_i^{lm}(\Xi).\tag{A42}$$

In order to evaluate the integrals efficiently and accurately, we use Gaussian grids in both latitude and longitude directions. Denoting the non-uniformly spaced Gaussian grid points in  $\phi$  by  $\phi_j$  and the corresponding Gaussian weights by  $w_j$ , a  $\phi$ -integral can be expressed as

$$I(\phi) = \int_{-\frac{\pi}{2}}^{\frac{\pi}{2}} d\phi f(\phi) \approx \sum_j w_j f(\phi_j). \quad (A43)$$

Similarly a  $\lambda$ -integral respectively involving a cosine and sine functions can be expressed as:

$$I_1(\lambda) = \int_0^{2\pi} d\lambda \cos m\lambda f(\lambda) \approx \sum_k w_k \cos m\lambda_k f(\lambda_k), \quad (A44)$$

$$I_2(\lambda) = \int_0^{2\pi} d\lambda \sin m\lambda f(\lambda) \approx \sum_k w_k \sin m\lambda_k f(\lambda_k), \quad (A45)$$

in which  $\lambda_k$  is the Gaussian grid in longitude and  $w_k$  is the corresponding weighting function. Using the expressions (A43-A45), the expansion coefficients for the height and the flow variables can be represented in Gaussian grids as:

$$a_r^{lm} = \frac{1}{\sqrt{\alpha_{lm}}} \sum_j w_j P_{lm}(\phi_j) \cos \phi_j \sum_{k=1}^{N_k} w_k \cos m\lambda_k h(\phi_j, \lambda_k), \quad (A46)$$

$$a_i^{lm} = \frac{1}{\sqrt{\alpha_{lm}}} \sum_j w_j P_{lm}(\phi_j) \cos \phi_j \sum_{k=1}^{N_k} w_k \sin m\lambda_k h(\phi_j, \lambda_k), \quad (A47)$$

$$b_r^{lm} = \sum_j w_j \cos \phi_j \{V_{lm}(\phi_j) \tilde{v}c_m(\phi_j) - W_{lm}(\phi_j) \tilde{u}s_m(\phi_j)\}, \quad (A48)$$

$$b_i^{lm} = \sum_j w_j \cos \phi_j \{W_{lm}(\phi_j) \tilde{u}c_m(\phi_j) + V_{lm}(\phi_j) \tilde{v}s_m(\phi_j)\} i, \quad (A49)$$

$$c_r^{lm} = \sum_j w_j \cos \phi_j \{V_{lm}(\phi_j) \tilde{u}c_m(\phi_j) + W_{lm}(\phi_j) \tilde{v}s_m(\phi_j)\}, \quad (A50)$$

$$c_i^{lm} = \sum_j w_j \cos \phi_j \{-W_{lm}(\phi_j) \tilde{v}c_m(\phi_j) + V_{lm}(\phi_j) \tilde{u}s_m(\phi_j)\}, \quad (A51)$$

in which

$$\begin{aligned} \tilde{u}c_m(\phi_j) &= \sum_{k=1}^{N_\lambda} \cos(\lambda_k m) u(\phi_j, \lambda_k), \\ \tilde{u}s_m(\phi_j) &= \sum_{k=1}^{N_\lambda} \sin(\lambda_k m) u(\phi_j, \lambda_k), \end{aligned}$$

$$\begin{aligned}\tilde{v}c_m(\phi_j) &= \sum_{k=1}^{N_\lambda} \cos(\lambda_k m) v(\phi_j, \lambda_k), \\ \tilde{v}s_m(\phi_j) &= \sum_{k=1}^{N_\lambda} \sin(\lambda_k m) v(\phi_j, \lambda_k).\end{aligned}$$

Swarztrauber (1996) solved the shallow-water equations in physical space evaluating nonlinear terms in spectral space. We will instead evolve the spectral coefficients following Hack & Jakob (1992), so we construct a semi-implicit time evolution scheme, because the time step utilized by explicit time differencing methods is limited by the speed of the fastest gravity wave. The semi-implicit time integration removes this constraint by treating terms that give rise to gravity waves implicitly, and the remaining terms explicitly.

Each of the Equations (A37-A42) has a linear term. We write all of these equations in centrally time differenced form and the linear term averaged over time  $\tau - 1$  and  $\tau + 1$ . We omit the superscript of  $lm$  from all the terms for focussing only on time evolution scheme.

$$\frac{1}{2\Delta_\tau} [b_r^{\tau+1} - b_r^{\tau-1}] = b_r^\tau(\Xi) - \sqrt{n(n+1)}d_r^\tau - G\sqrt{n(n+1)}\left(\frac{a_r^{\tau+1} + a_r^{\tau-1}}{2}\right), \quad (\text{A52})$$

$$\frac{1}{2\Delta_\tau} [b_i^{\tau+1} - b_i^{\tau-1}] = b_i^\tau(\Xi) - \sqrt{n(n+1)}d_i^\tau - G\sqrt{n(n+1)}\left(\frac{a_i^{\tau+1} + a_i^{\tau-1}}{2}\right), \quad (\text{A53})$$

$$\frac{1}{2\Delta_\tau} [a_r^{\tau+1} - a_r^{\tau-1}] = a_r^\tau(\Psi) + \sqrt{n(n+1)}\left(\frac{b_r^{\tau+1} + b_r^{\tau-1}}{2}\right), \quad (\text{A54})$$

$$\frac{1}{2\Delta_\tau} [a_i^{\tau+1} - a_i^{\tau-1}] = a_i^\tau(\Psi) + \sqrt{n(n+1)}\left(\frac{b_i^{\tau+1} + b_i^{\tau-1}}{2}\right). \quad (\text{A55})$$

Equations (A52) and (A54) are coupled, similarly Equations (A53) and (A55) are also coupled. We write Equations (A52) and (A54) in matrix form as

$$\begin{pmatrix} g\Delta_\tau\sqrt{n(n+1)} & 1 \\ 1 & -\Delta_\tau\sqrt{n(n+1)} \end{pmatrix} \begin{pmatrix} a_r^{\tau+1} \\ b_r^{\tau+1} \end{pmatrix} \quad (\text{A56})$$

$$= \begin{pmatrix} 2\Delta_\tau \left( b_r^\tau(\Xi) - \sqrt{n(n+1)}d_r^\tau \right) - g\Delta_\tau\sqrt{n(n+1)}a_r^{\tau-1} + b_r^{\tau-1} \\ 2\Delta_\tau a_r^\tau(\Psi) + \Delta_\tau\sqrt{n(n+1)}b_r^{\tau-1} + a_r^{\tau-1} \end{pmatrix} \quad (\text{A57})$$

which can be written as

$$a_r^{\tau+1} = \frac{1}{[g\Delta_\tau^2 n(n+1) + 1]} \left[ a_r^{\tau-1} \{-g\Delta_\tau^2 n(n+1) + 1\} + 2\Delta_\tau \left\{ a_r^\tau(\Psi) - \Delta_\tau n(n+1)d_r^\tau + (b_r^{\tau-1} + \Delta_\tau b_r^\tau(\Xi)) \sqrt{n(n+1)} \right\} \right] \quad (\text{A58})$$

$$b_r^{\tau+1} = \frac{1}{[g\Delta_\tau^2 n(n+1) + 1]} \left[ b_r^{\tau-1} \{-g\Delta_\tau^2 n(n+1) + 1\} - 2\Delta_\tau \left\{ -b_r^\tau(\Xi) + (d_r^\tau + ga_r^{\tau-1} + g\Delta_\tau a_r^\tau(\Psi)) \sqrt{n(n+1)} \right\} \right] \quad (\text{A59})$$

Similarly, Equations (A53) and (A55) can be written as

$$a_i^{\tau+1} = \frac{1}{[g\Delta_\tau^2 n(n+1) + 1]} \left[ a_i^{\tau-1} \{-g\Delta_\tau^2 n(n+1) + 1\} + 2\Delta_\tau \left\{ a_i^\tau(\Psi) - \Delta_\tau n(n+1)d_i^\tau + (b_i^{\tau-1} + \Delta_\tau b_i^\tau(\Xi)) \sqrt{n(n+1)} \right\} \right] \quad (\text{A60})$$

$$b_i^{\tau+1} = \frac{1}{[g\Delta_\tau^2 n(n+1) + 1]} \left[ b_i^{\tau-1} \{-g\Delta_\tau^2 n(n+1) + 1\} - 2\Delta_\tau \left\{ -b_i^\tau(\Xi) + (d_i^\tau + ga_i^{\tau-1} + g\Delta_\tau a_i^\tau(\Psi)) \sqrt{n(n+1)} \right\} \right] \quad (\text{A61})$$

We discretize the Equations (A41) and (A42) in time for explicit evolution:

$$c_r^{\tau+1} = c_r^\tau + \Delta_\tau c_r^{\tau-1}(\Xi) \quad (\text{A62})$$

$$c_i^{\tau+1} = c_i^\tau + \Delta_\tau c_i^{\tau-1}(\Xi) \quad (\text{A63})$$

We have presented above all the equations we need to do time integration. At each time step we integrate equations (A58-63). The details of the time evolution in each time-advancement involve sequentially the following steps:

1. From  $b_r^{lm}$ ,  $b_i^{lm}$ ,  $c_r^{lm}$  and  $c_i^{lm}$  compute  $u$  and  $v$  in  $(\theta, \phi)$  Gaussian grid using Equations (A9) and (A10).
2. From  $a_r^{lm}$  and  $a_i^{lm}$  compute  $h$  in  $(\theta, \phi)$  Gaussian grid using Equation (A1).
3. From  $b_r^{lm}$ ,  $b_i^{lm}$ ,  $c_r^{lm}$  and  $c_i^{lm}$  compute  $\zeta$  and  $\delta$  in  $(\theta, \phi)$  Gaussian grid using Equations (A15) and (A16).
4. From  $u$ ,  $v$ ,  $\zeta$  and  $\delta$  computed in steps 1 and 2, and  $\omega_c$  given, compute  $\Xi_u$  and  $\Xi_v$  using Equations (A19) and (A20).
5. Substitute  $\Xi_u$  and  $\Xi_v$ , obtained from step 4, in Equations (A11-A14) with  $u$  and  $v$  respectively to evaluate  $b_r^{lm}(\Xi)$ ,  $b_i^{lm}(\Xi)$ ,  $c_r^{lm}(\Xi)$  and  $c_i^{lm}(\Xi)$ .

6. Compute  $\frac{1}{2}(u^2 + v^2)$  from the already computed values of  $u$  and  $v$  from step 1, and then using sequentially the Equations (A32), (A17), (A18), (A3) and (A4), compute  $d_r^{lm}$  and  $d_i^{lm}$ .
7. Compute the gradients of  $\frac{1}{2}(u^2 + v^2)$  in  $(\theta, \phi)$  Gaussian grids using  $d_r^{lm}$  and  $d_i^{lm}$  from step 6, using Equations (A17) and (A18).
8. Compute the gradients of  $h$  in  $(\theta, \phi)$  Gaussian grids using  $a_r^{lm}$  and  $a_i^{lm}$  in Equations (A17) and (A18).

The above steps constitute the complete computations of right hand side of Equations (A37-A42). Using the right hand side we compute  $b_r^{lm}$ ,  $a_r^{lm}$ ,  $b_i^{lm}$ ,  $a_i^{lm}$  for the next time advancement from Equations (A58-A61), and  $c_r^{lm}$  and  $c_i^{lm}$  from Equations (A62) and (A63). We repeat the above eight steps forward as long as we want to continue the time marching.

## REFERENCES

- Arlt, R., Sule, A. & Rüdiger, G. 2005, A&A, 441, 1171
- Cally, P. S. 2001, SolP, 199, 231
- Cally, P. S., Dikpati, M. & Gilman, P. A. 2003, ApJ, 582, 1190
- Cally, P. S., Dikpati, M. & Gilman, P. A. 2004, ASP Conf. Proc. 219, p.541, on “Stars as suns : activity, evolution and planets” IAU Symposium, eds. A.K. Dupree and A.O. Benz. San Francisco, CA
- Chan, K. H., Liao, X. & Zhang, K. 2008, ApJ, 682, 1392
- Charbonneau, P., Dikpati, M. & Gilman, P. A. 1999, ApJ, 526, 523
- Dikpati, M., Cally, P. S. & Gilman, P. A. 2004, ApJ, 610, 597
- Dikpati, M. & Gilman, P. A. 1999, ApJ, 512, 417
- Dikpati, M. & Gilman, P. A. 2001, ApJ, 551, 536
- Dikpati, M. & Gilman, P. A. 2005, ApJ, 653, L193
- Dikpati, M., Gilman, P. A. & Rempel, M. 2003, ApJ, 596, 680
- Dziembowski, W. & Kosovichev, A. G. 1987, ACTA Astronomica, 37, 313



- Fan, Y., Zweibel, E. G., Linton, M. G. & Fisher, G. H. 1999, *ApJ*, 521, 460
- Garaud, P. 2001, *MNRAS*, 324, 68
- Gelb, A. & Gleeson, J. P. 2001, *Monthly Weather Rev.*, 129, 2346
- Gilman, P. A. & Fox, P. A. 1997, *ApJ*, 484, 439
- Gilman, P. A. & Dikpati, M. 2002, *ApJ*, 576, 1031
- Gilman, P. A., Dikpati, M. & Miesch, M. S. 2007, *ApJS*, 170, 203
- Hack, J. J. & Jakob, R. 1992, NCAR Technical Note NCAT/TN-343+STR
- Hollerbach, R. & Cally, P. S. 2009, *Sol. Phys.*, 260, 251
- Huang, R. X. & Pedlosky, J. 1998, *J. of Physical Oceanography*, 29, 779
- Hurlburt, H. E. & Hogan, P. J. 2008, *Dynamics of Atmospheres and Oceans*, 45, 71
- Miesch, M. S., Gilman, P. A. & Dikpati, M. 2007, *ApJS*, 168, 337
- Pedlosky, J. 1987, *Geophysical Fluid Dynamics* (New York:Springer), 710
- Philander, S. G. & Fedorov, A. 2003, *Ann. Rev. of Earth and Planetary Science*, 31, 579
- Poulin, S. G. & Flierl, A. 2003, *J. Phys. Oceanogr.*, 33, 2173
- Rempel, M. & Dikpati, M. 2003, *ApJ*, 584, 524
- Swarztrauber, P. N. 1996, *Monthly Weather Rev.*, 124, 730
- Watson, M. 1981, *Geophys. Astrophys. Fluid Dyn.*, 16, 285
- Zhang, K., Liao, X. & Schubert, G. 2003, *ApJ*, 585, 1124